Physical and chemical strain-hardening during faulting in poorly lithified sandstone: The role of kinematic stress field and selective cementation

THE GEOLOGICAL SOCIETY OF AMERICA®

Physical and chemical strain-hardening during faulting in poorly lithified sandstone: The role of kinematic stress field and selective cementation

Mattia Pizzati[1,†], Fabrizio Balsamo[1], Fabrizio Storti[1], and Paola Iacumin[2]

[1]*Natural and Experimental Tectonics Research Group, Department of Chemistry, Life Sciences, and Environmental Sustainability, University of Parma, I-43124 Parma, Italy*

[2]*Department of Chemistry, Life Sciences, and Environmental Sustainability, University of Parma, I-43124 Parma, Italy*

ABSTRACT

In this work, we report the results of a multidisciplinary study describing the structural architecture and diagenetic evolution of the Rocca di Neto extensional fault zone developed in poorly lithified sandstones of the Crotone Basin, Southern Italy. The studied fault zone has an estimated displacement of ~90 m and consists of: (1) a low-deformation zone with subsidiary faults and widely spaced deformation bands; (2) an ~10-m-wide damage zone, characterized by a dense network of conjugate deformation bands; (3) an ~3-m-wide mixed zone produced by tectonic mixing of sediments with different grain size; (4) an ~1-m-wide fault core with bedding transposed into foliation and ultracomminute black gouge layers. Microstructural investigations indicate that particulate flow was the dominant early-stage deformation mechanism, while cataclasis became predominant after porosity loss, shallow burial, and selective calcite cementation. The combination of tectonic compaction and preferential cementation led to a strain-hardening behavior inducing the formation of "inclined conjugate deformation band sets" inside the damage zone, caused by the kinematic stress field associated with fault activity. Conversely, conjugate deformation band sets with a vertical bisector formed outside the damage zone in response to the regional extensional stress field. Stable isotope analysis helped in constraining the diagenetic environment of deformation, which is characterized by mixed marine-meteoric signature for cements hosted inside the damage zone, while it progressively becomes more meteoric moving outside the fault zone. This evidence supports the outward propagation of fault-related deformation structures in the footwall damage zone.

†mattia.pizzati@studenti.unipr.it.

INTRODUCTION

Understanding the mechanical behavior of faulted sediments and high-porosity sandstones has a primary impact on the improvement of conceptual models of faulting at very shallow depth, including both coseismic rupture propagation and creeping along faults (Scholz, 1998; Gratier et al., 2011; Ozawa et al., 2011; Yamaguchi et al., 2011; Imanishi et al., 2012; Kodaira et al., 2012; Fagereng et al., 2014). This is particularly true for the response of materials to incremental deformation, specifically whether sediments or rocks have a strain-hardening or softening behavior with shearing and what are the controlling factors. Strain-hardening characterizes materials that show an increasing resistance to deformation with progressive increments of stress and strain (e.g., Fossen, 2010). It occurs within the inelastic deformation field and is responsible for the shift to higher stress-strain values of the yield point of the deforming material (Mair et al., 2000). On the contrary, strain-softening causes a diminishing of mechanical properties of the deformed material, facilitating deformation along discrete surfaces (Fossen, 2010). Strain-hardening in granular media such as high-porosity sandstones and poorly lithified sediments promotes the transfer of deformation to the surrounding undeformed sediments, rather than persisting on pre-existing deformation structures, which become stronger and less easily re-activated (Aydin and Johnson, 1978; Mair et al., 2000; Fossen et al., 2018). Such deformation structures typically consist of deformation bands of different types and geometries (e.g., Friedman and Logan, 1973; Aydin, 1978; Antonellini et al., 1994; Cashman and Cashman, 2000; Wilson et al., 2003; Rotevatn et al., 2008; Torabi and Fossen, 2009; Fossen et al., 2018; Philit et al., 2018).

Progressive strain-hardening behavior commonly leads to the formation of clusters of closely spaced deformation bands that, after reaching a threshold thickness, eventually fail internally to develop preferential slip surfaces that accommodate additional strain (Aydin and Johnson, 1978, 1983; Antonellini et al., 1994; Soliva et al., 2016). The development of discrete slip surfaces inside a cluster of deformation bands may be related to transient strain-softening behavior, which allows the displacement to be accommodated along narrow structures (Mair et al., 2000; Nicol et al., 2013). Strain-hardening and softening are therefore responsible for early-stage delocalization of deformation, and late-stage localization on discrete slip surfaces, respectively. Shear localization in loose materials is expected to increase the kinematically induced shear stress field (e.g., Davis et al., 2012) along the fault zone to eventually overcome the strength of sediments and produce shear-related deformation structure arrays (Logan et al., 1979; Hancock, 1985; Sylvester, 1988).

Fault damage zones form as a response to the accumulated deformation due to delocalization of strain (Kim et al., 2004; Mitchell and Faulkner, 2009; Choi et al., 2016). Inside damage zones, stratigraphic features are often preserved and deformation bands are abundant, surrounding thin fault cores, where most of the fault slip is accommodated (Shipton and Cowie, 2001, 2003; Davatzes et al., 2005; Williams et al., 2017). When fault displacement exceeds bedding thickness, mixed zones may form between fault cores and damage zones (Heynekamp et al., 1999; Rawling and Goodwin, 2006; Loveless et al., 2011).

Transition from shear delocalization to localization may correspond to a switch from dominant aseismic slip and possibly slow earthquakes, typically associated with deformation banding (Fossen et al., 2018), to coseismic slip producing thin layers of black gouge (Balsamo et al., 2014; Ujiie and Kimura, 2014). However,

 https://doi.org/10.1130/B35296.1; 14 figures; Data Repository item 2019349.

in some cases, black gouges can form in pristine sediments without the strain-hardening effect caused by deformation bands in damage zones (Balsamo and Storti, 2011). Moreover, deformation band development is not restricted to low-slip rate deformation, but can also occur in response to coseismic slip along faults affecting high-porosity siliciclastic rocks (Cashman and Cashman, 2000).

Faulting associated with deformation bands influences the hydrological behavior of deformed rocks and provides barriers to fluid flow, especially toward fluids directed orthogonal to the band surfaces (e.g., Antonellini and Aydin, 1994; Main et al., 2000; Ogilvie and Glover, 2001; Sternlof et al., 2004; Balsamo and Storti, 2010; Ballas et al., 2012; Bense et al., 2013). The barrier role is typically less pronounced in a direction parallel to the strike of the deformation bands (Fossen and Bale, 2007). However, the hydrological role can be influenced by the saturation conditions of the sediments or rocks involved in the deformation; deformation bands developed under fully saturated conditions are likely to constitute barriers, while those formed in partial or non-saturated media may act as partial conduits (Sigda et al., 1999; Sigda and Wilson, 2003).

At the deformation band scale, pore collapse produced by both failure of sedimentary grain packing and grain size reduction by cataclasis, can favor selective cementation along deformation bands and fault cores (Antonellini et al., 1994; Eichhubl et al., 2009; Balsamo et al., 2012; Philit et al., 2015; Williams et al., 2015; Del Sole and Antonellini, 2019). Such a preferential structural diagenesis can dramatically alter the mechanical behavior of deformation bands and fault zones. It follows that, in many cases, a combination of physical and chemical syn-kinematic processes drives the evolution of strain-hardening and softening in high-porosity sediments during faulting and, hence, the evolution of fault frictional properties (Antonellini et al., 1994; Mair et al., 2000; Skurtveit et al., 2015).

In the available scientific literature a few works were addressed to study the interaction between deformation and related diagenetic processes (i.e., cementation), occurring at shallow burial conditions (Eichhubl et al., 2009; Philit et al., 2015; Williams et al., 2015). In particular, the role of syn-kinematic cementation in varying the mechanical and frictional properties of deformed rocks and driving the deformation style and pattern is still poorly constrained and understood. Concerning the evolution of the overall fault zone structure, there are uncertainties relative to the time of development of the structural domains composing fault zones.

To shed light and provide answers to the aforementioned open questions, we studied in detail the cross-sectional architecture of the Rocca di Neto extensional fault zone, developed in arkosic to lithic-arkosic high-porosity sandstone of the Crotone Basin, in Southern Italy. The basin provides very good exposures of extensional fault zones affecting loose sandstone, and many of them are characterized by abundant occurrence of selective cementation in the form of carbonate concretions both in damage zones and in fault cores (Balsamo et al., 2012). The structure of the Rocca di Neto fault was described by mesoscopic and microscopic investigations, whereas the cementation history was constrained by petrographic and stable isotope analyses, to determine the overall evolution of the fault zone during slip accommodation and basin exhumation.

GEOLOGICAL FRAMEWORK

The Rocca di Neto extensional fault zone is located in the Crotone forearc basin, which developed since Middle Miocene times during the SE-ward migration of the Calabrian Arc, in the Southern Apennines of Italy (Knott and Turco, 1991; Van Dijk and Scheepers, 1995; Van Dijk et al., 2000; Zecchin et al., 2004, 2012) (Figs. 1A and 1B). The interaction between

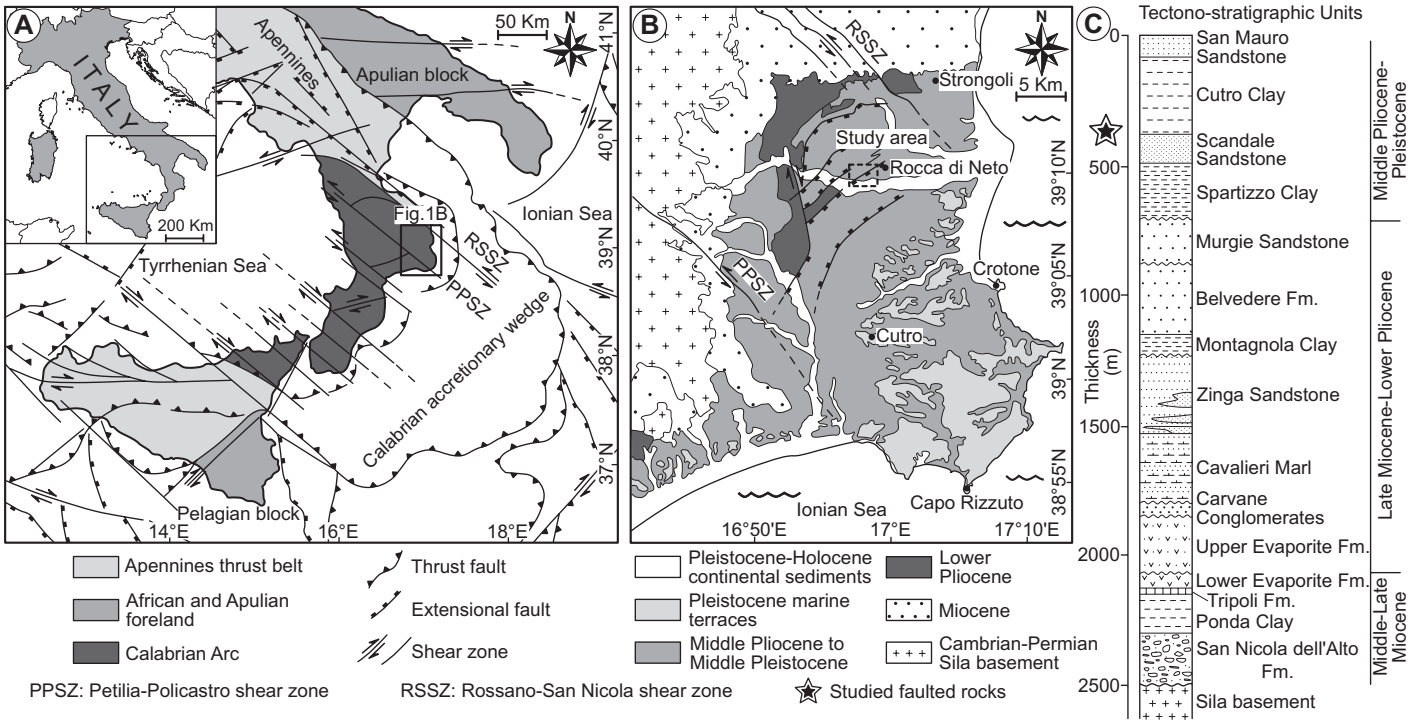

Figure 1. (A) Regional setting of the Calabrian Arc (Southern Italy) and related accretionary wedge (after Van Dijk et al., 2000). (B) Geological map of the Crotone Basin (modified after Zecchin et al., 2012). (C) Stratigraphic succession of the entire Crotone Basin (modified after Balsamo et al., 2012). Fm—Formation.

subduction of the Adria-Ionian plate underneath the European plate, and back-arc spreading in the Tyrrhenian Sea, was responsible for the onset of different tectonic regimes during basin formation and infilling (Polonia et al., 2011; Reitz and Seeber, 2012; Massari and Prosser, 2013). Since Lower Pliocene times, the basin underwent at least five subsidence-uplift cycles, induced by the interplay between subduction-related contraction and back-arc extension (Van Dijk, 1994; Van Dijk and Scheepers, 1995; Ferranti et al., 2009; Zecchin et al., 2012; Massari and Prosser, 2013). The dominant extensional tectonic regime, active since Middle Pleistocene times, was likely induced by temporary cessation or slowing down of subduction underneath the Calabrian Arc (Antonioli et al., 2006; Zecchin et al., 2012).

The onshore portion of the Crotone Basin is bounded to the north and to the south by the NW-SE–trending Rossano-San Nicola and Petilia-Policastro left-lateral, strike-slip shear zones (Van Dijk, 1994; Zecchin et al., 2004; Galli and Scionti, 2006) (Fig. 1B). In the central part of the basin, several NE-SW–trending extensional fault zones are interpreted to have formed during the last extensional event (Antonioli et al., 2006; Massari and Prosser, 2013).

Basin infilling started during the Middle Miocene and the sedimentary succession recorded sedimentation occurring in depositional environments spanning from fluvial to shallow marine (shoreface-offshore). The entire succession has a maximum thickness of 2500 m and is mainly composed of sandstones, conglomerates, clays, gypsum, and to a lesser extent siliceous sediments (Fig. 1C). Sedimentation was strongly influenced by fluctuations of sea level due to the transgressive and regressive cycles that have occurred since the Middle Miocene, leading to rapidly shifting depositional environments (Zecchin et al., 2012).

During the entire infilling history of the Crotone Basin, siliciclastic sediment supply was mainly provided by the erosion of the metamorphic basement rocks exposed in the adjacent Sila Massif since the first stages of basin formation (Van Dijk et al., 2000; Zecchin et al., 2004, 2012). The Rocca di Neto fault zone affects the most recent portion of the stratigraphic succession, juxtaposing the Cutro clay in the hanging wall, against the poorly lithified Scandale sandstone in the footwall (Fig. 1C). In particular, we focused on deformation structures well exposed in the fault footwall. The Scandale sandstone is mainly composed of quartz, K-feldspar, plagioclase, and lithic fragments. Lithics mainly consist of gneiss and granitic rock fragments; biotite and muscovite micas also occur, but typically constitute less than 5% of the grains. Other accessory minerals are Fe-Ti oxides, detrital and biogenic calcite (shell fragments). Cement is generally absent and intergranular porosity is high. The studied sandstones are heterolithic and consist of medium-fine and coarse-grained alternating layers, with immature texture and moderate to good sorting (Balsamo and Storti, 2010).

ANALYTICAL METHODS

To investigate on the type and density of deformation bands and faults exposed in the footwall of the Rocca di Neto extensional fault zone, we constructed a 63 m long, detailed geological cross-section throughout the entire fault footwall. The CF parameter was used to quantify deformation band density (Soliva et al., 2016). It is defined as follows:

$$CF = \sqrt{\frac{\sum f_i^2}{\sum f_i} - f_{av}}, \quad (1)$$

where CF stands for clustering factor, f_i is the density of bands per meter at the i^{th} meter of the scan-line, and f_{av} is the average band density along the entire scan-line.

Hand samples were collected in different positions along the fault zone to obtain 55 polished thin sections impregnated with blue-dyed resin to facilitate porosity estimations (see Data Repository Table DR1 for the position of the samples in the fault zone).[1] Among them, 25 thin sections were obtained from carbonate concretion samples and stained with a solution of alizarin red S and potassium ferricyanide to determine the nature of carbonate cement (calcite vs dolomite; Dickson, 1966). Petrographic investigations on thin sections were performed with a standard petrography microscope (Zeiss Axioplan 2) and on scanned high-resolution images of the entire thin section area (Nikon Super CoolScan 5000). A cold cathodoluminescence apparatus (CITL Mk5-2 operating setting 250 µA and 10 kV) was used to investigate in detail generations and spatial distribution of cements. Detailed photomicrographs of cement and microstructures were acquired with a JEOL JSM 6400 scanning electron microscope (with operating setting 240 nA and 20 kV).

Carbon and oxygen stable isotope analysis was performed on small powder amounts extracted from concretion fresh cuts using a dental drill. Two sampling transects were made on each concretionary body, parallel and orthogonal to the basal surface, respectively. Sampling distance was 1.0 cm for surface-parallel transects and 1.0 or 0.5 cm for surface-orthogonal ones, depending on concretion thickness. A total of 324 isotopic pair data was obtained. Carbonate powders were reacted with 100% phosphoric acid at a constant temperature of 70 °C. An additional CO_2 reference gas (pure Carrara marble) with known isotopic ratio was analyzed during the measurements to determine the $\delta^{13}C$ and $\delta^{18}O$ values. Samples were analyzed with a Thermo Finnigan DELTA plus XP mass spectrometer coupled with a Thermo Finnigan GasBench II gas preparation and sample introduction device. Both $\delta^{13}C$ and $\delta^{18}O$ values are referred to the international standard V-PDB (Vienna Pee Dee belemnite). The analytical precision upon $\delta^{13}C$ determination was 0.10‰ V-PDB, while on $\delta^{18}O$ it was 0.15‰. The uncertainty was 0.15‰ for carbon and 0.20‰ for oxygen isotopes, respectively (complete isotopic data set is provided in Data Repository Table DR2; see footnote 1).

The relative rock strength was measured with a Schmidt hammer (Proceq Instruments, N-type configuration hammer, with an impact energy of 2.207 Nm). The instrument provides the Q rebound value calculated as follows:

$$Q = 100 \times \frac{Energy(recovered)}{Energy(impact)}, \quad (2)$$

where Q indicates the output rebound value, $Energy_{(recovered)}$ is the remaining after the elastic rebound and $Energy_{(impact)}$ is the input impact strength. A total of 30 rebound values were collected on each deformation band or concretionary body. To ensure measurement accuracy, selected areas were deeply polished with a corundum abrasive tool in order to remove alteration haloes and reduce surface roughness (Katz et al., 2000; Demirdag et al., 2009). Measurements were made keeping the Schmidt hammer orthogonal to the reference surface, being the instrument equipped with an automatic correction tool for inclination. Analysis of Q value was made after discarding the lower half of data distribution (Katz et al., 2000).

FAULT ZONE STRUCTURE

The NE-SW–trending Rocca di Neto extensional fault zone is located ~1 km southwestward from the eponymous village and is exposed in a dismissed quarry area and along a road cut (Fig. 2A). These outcrops provide an excellent exposure of the footwall of the fault, while the hanging wall side (developed in the clayish sediments pertaining to the Cutro clay Formation) is almost completely covered by debris. The maximum displacement of the Rocca

[1]GSA Data Repository item 2019349, Complete isotopic data, concretion samples, statistical analysis, and back-calculation of $\delta^{18}O$ of parental fluids, is available at http://www.geosociety.org/datarepository/2019 or by request to editing@geosociety.org.

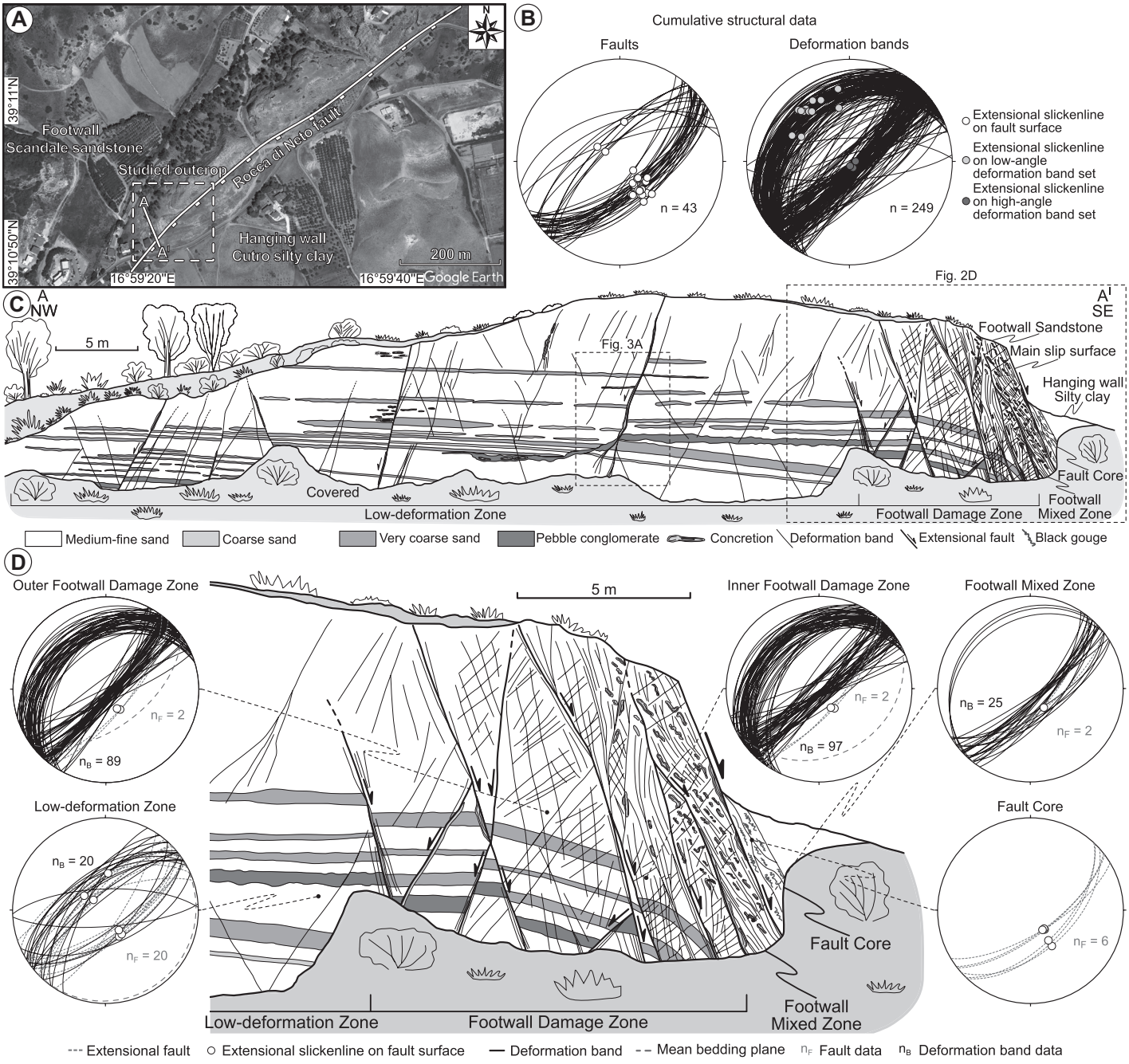

Figure 2. (A) Satellite image (Google Earth) of the investigated Rocca di Neto fault zone (Crotone Basin, Southern Italy) with the trace of the master fault and the position of the studied outcrop. (B) Cumulative structural data regarding faults and deformation bands through the footwall of the Rocca di Neto fault zone (Schmidt lower hemisphere projection). (C) Detailed geological cross-section of the fault zone with the identified structural domains. (D) Detail of the fault domains, with stereonets plotting the structural data (Schmidt lower hemisphere projection).

di Neto fault is estimated to be 80–90 m, on the basis of stratigraphic constraints. The entire footwall side of the fault zone developed within the Scandale sandstone is characterized by the occurrence of deformation bands, deformation band clusters, and slip surfaces (Figs. 2B and 2C). Deformation bands far from the master slip surface mainly occur in scattered conjugate pairs with vertical bisectors (Figs. 2C and 2D). Low-displacement antithetic faults also occur (Figs. 2 and 3A). In the outer and inner footwall damage zone, and in the footwall mixed zone, deformation bands form dense networks of conjugate pairs (DB1 and DB2) with inclined bisectors (Fig. 2D). Approaching the master slip surface, a third set of deformation bands (DB), oriented parallel to subsidiary faults, also occurs (Figs. 3B–3D).

Low-Deformation Zone

By low-deformation zone (LDZ) we refer to the sector outside the footwall damage zone, affected by background deformation.

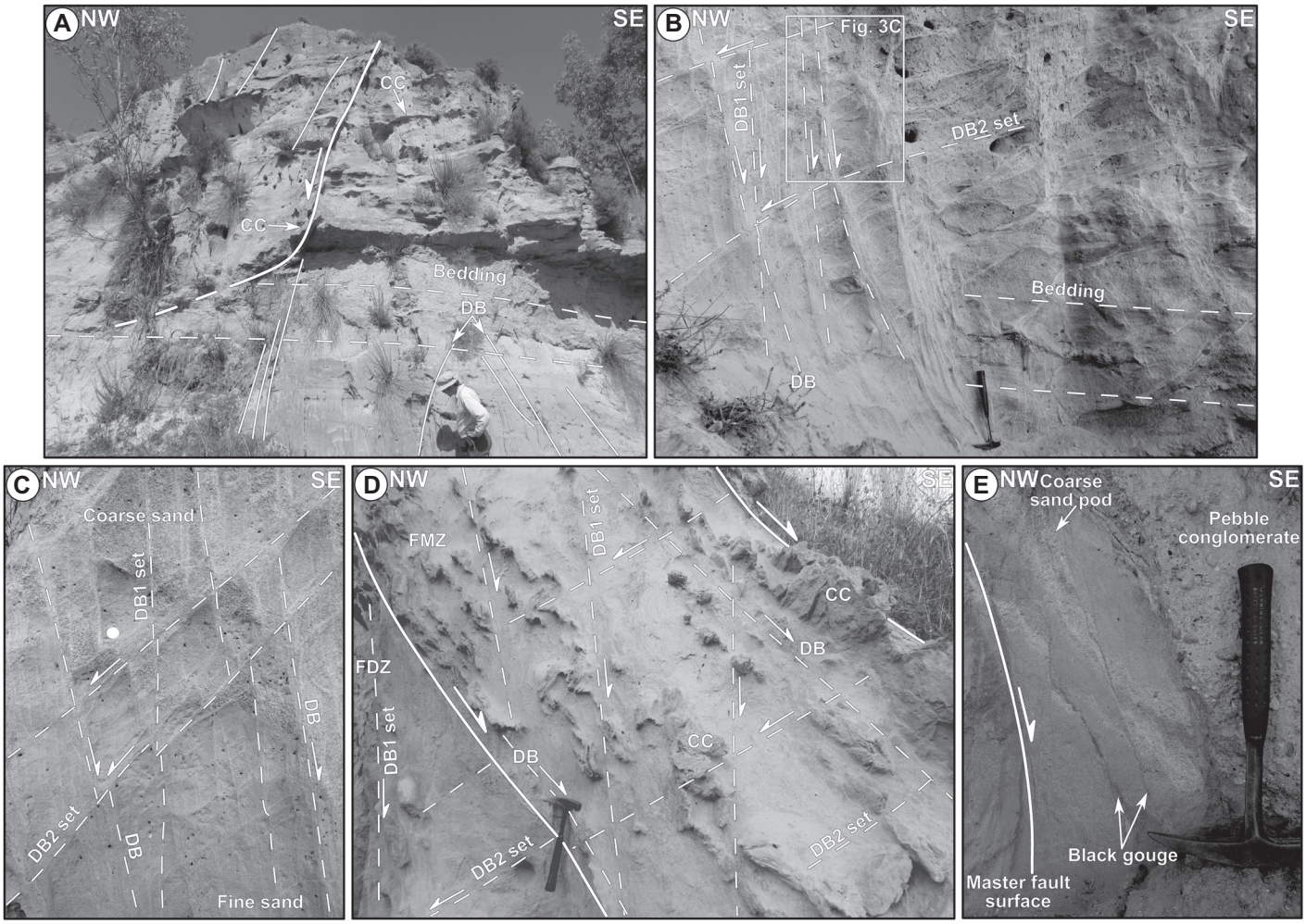

Figure 3. Main outcrop structural features of the fault domains along the footwall of the Rocca di Neto fault zone. (A) Low-displacement fault within the low-deformation zone. A few, widely spaced deformation bands are also present. Carbonate concretions are present both along minor faults and parallel to bedding. (B) Conjugate deformation bands within the footwall damage zone. (C) Detail of the deformation band sets with mutual cross-cut relationship. (D) Boundary between the footwall damage zone (FDZ) and footwall mixed zone (FMZ). (E) Fault core with the main slip surface on the left side of the figure, foliated sandstone and black gouges. DB—fault-parallel deformation band; DB1—high-angle deformation band; DB2—low-angle deformation band; CC—carbonate concretion; FDZ—footwall damage zone; FMZ—footwall mixed zone.

There, bedding has a slight dip (~5°) toward SE (Figs. 2C and 3A). According to the scan-line, this domain is ~48 m wide as indicated by the gentle slope of the best-fit line of the cumulated deformation band frequency (Fig. 4). The LDZ is characterized by the presence of widely spaced conjugate deformation bands with displacement generally <1–2 cm, and minor conjugate faults, with displacement <15–20 cm (Fig. 2C). Deformation bands and subsidiary faults are arranged in conjugate patterns making a mean acute dihedral angle of 48° (α in Fig. 5A). The antithetic and synthetic sets describe an angle of 47° and 2° with the master fault, respectively (Fig. 5A). The mean density of deformation bands is 3.5 m^{-1}, with a peak value of 17 m^{-1} (Fig. 4). Higher values are measured in the vicinity of three antithetic faults cutting through the entire quarry wall and characterized by sharp surfaces and displacement values between 0.5 and 1.5 m (Fig. 3A). Locally, slip surfaces show preferential cementation and slickenlines. The deformation band clustering factor (CF) calculated for the LDZ yields a value of 0.62 (Fig. 4).

Footwall Damage Zone

In the footwall damage zone (FDZ) bedding is still recognizable, but is locally displaced by faults (Fig. 2C). Within the innermost part of the footwall damage zone, bedding is tilted in fault blocks, and steeply dragged (dip value of ~50°) by a high-displacement fault located at the footwall damage zone-mixed zone boundary (Fig. 2D). The transition to the low-deformation domain occurs as a progressive decrease of conjugate deformation band and fault density (Fig. 4). Subsidiary fault zones are 10–30 cm thick, with well-developed slip surfaces and a set of sub-parallel deformation bands adjacent to them (DB in Figs. 3C and 3D). These fault zones have greater displacement approaching the master slip surface.

The total width of the FDZ is ~10 m, as constrained by the linear fit of cumulated deformation band frequency showing steeper slope compared to the low-deformation zone (Fig. 4). In particular, the mean density of deformation bands is 6.7 m^{-1}, with a maximum value of 11 m^{-1}. The deformation band clustering factor yields a value of 1.39, i.e., more than twice

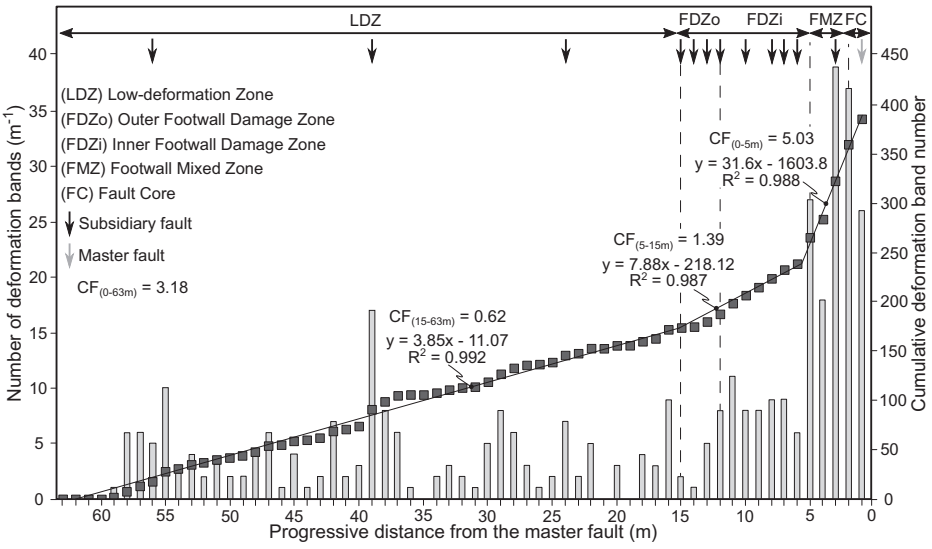

Figure 4. Linear scan-line along the footwall side of the Rocca di Neto fault zone. Number of deformation bands is reported both as cumulative and non-cumulative number. The cumulative band number of the structural domains is fitted by linear functions with different slopes. CF—clustering factor (Soliva et al., 2016).

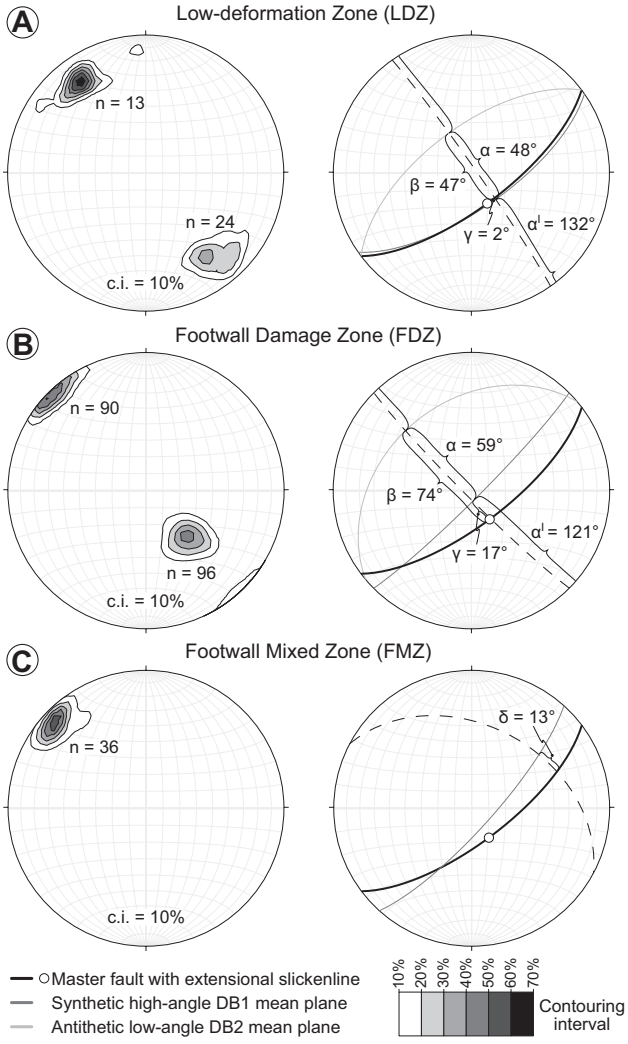

Figure 5. Stereonets (Schmidt lower hemisphere projection) with contouring of poles to deformation band planes performed on data collected from different structural domains along the Rocca di Neto fault zone. (A) Deformation band data from the low-deformation zone. (B) Deformation band data from the footwall damage zone. (C) Deformation band data from the footwall mixed zone. Mean deformation band planes are calculated from the maximum pole density. Relationships between deformation bands and main fault are reported as angles. α-α^{I}—acute and obtuse dihedral angles described by conjugate deformation bands; β—angle between the master fault and antithetic bands; γ—angle between the master fault and synthetic bands; δ—angle between the master fault and fault-parallel bands. c.i.—contouring interval.

that in the LDZ. Based on deformation band density, an inner (~7 m wide) and outer (~3 m wide) footwall damage zone can be identified (Fig. 4).

Deformation bands are organized in two conjugate sets (Fig. 3B): the first set (DB1), at high-angle to bedding, is synthetic with respect to the master slip surface, while the second one (DB2), at low-angle to bedding, has antithetic shear sense (Figs. 2D and 3C). Deformation bands show mutually cross-cut relationship and occur as single elements or as clusters of anastomosing bands (Fig. 3C). Along single deformation bands, displacement rarely exceeds a few centimeters, while thick clusters of bands may show an offset up to 20–25 cm. Conjugate deformation bands form an acute dihedral angle of 59° (Fig. 5B). The antithetic and synthetic sets describe an angle of 74° and 17° with the trace of the master slip surface, respectively (Fig. 5B).

Footwall Mixed Zone

In the footwall mixed zone (FMZ), bedding is almost completely transposed into foliation and only locally is still recognizable and displays a high dip angle. The FMZ consists of a 2–3-m-wide domain bounded by a synthetic fault zone both on the damage zone and on the fault core side (Figs. 2D and 3D). It is characterized by closely spaced, fault-parallel deformation bands with a mean density of 28 m^{-1}, with a peak value of 39 m^{-1} (Fig. 4). Close to the bounding fault zones, deformation bands are characterized by greenish colors and are thicker compared to those farther away from the two fault zones. In this structural domain the deformation band clustering factor value is 5.03 and the mean angle that deformation bands form with the master slip surface is 13° (Fig. 5C).

Fault Core

The fault core (FC) is a 1–2-m-wide body where most of the displacement is accommodated and deformation intensity is higher (Figs. 2D and 3E). It is composed of foliated medium-fine sand layers, alternating with coarse sand pods as remnants of the transposed original bedding (Fig. 3E). The footwall side of the fault core is bounded by the master slip surface showing extensional slickenlines, whereas the hanging wall side is mostly covered by debris. Close to the master slip surface, numerous black-dark green gouge layers are present. Many of them have a straight geometry, parallel to the master slip surface, while others are gently folded (Fig. 3E). Fault-parallel deformation bands also occur, as well as conjugate sets. The mean band density is 31.5 m^{-1}, with a maximum value of 37 m^{-1}

(Fig. 4). Deformation bands and gouges mutually cross-cut each other.

MICROSTRUCTURAL ANALYSIS

Deformation bands developed within the low-deformation zone, outside the fault footwall, usually show grain packing re-organization and incipient fragmentation of coarse grains, without evidence of significant grain rotation and cataclasis (Fig. 6A). Conjugate deformation bands inside the footwall damage zone display evidence for grain rotation, grain size reduction, and preferential orientation of grain major axes (Fig. 6B), even for millimetric displacements. Fault-parallel deformation bands are characterized by significant grain size reduction (Fig. 6C). Within the footwall mixed zone, fault-parallel deformation bands are thicker than those in the footwall damage zone and show extremely sharp boundaries at the thin section scale (Fig. 6D). Grain size reduction is not uniform, but is enhanced in ~250-µm-thick slip zones located in the central sectors of the deformation bands (Fig. 6D). Such crushed cores show a fine-grained brown matrix surrounding survivor quartz grains. The matrix is almost completely composed of crushed feldspar and plagioclase grains, fine particles of former calcite cement, and less abundant quartz chips.

High-strain fault-parallel deformation bands locally include ultra-comminute layers. They are typically asymmetric and show discontinuous gradients of grain size reduction organized in thin domains paralleling the deformation band boundaries, and are characterized by the preferential alignment of grains to produce a foliation (Fig. 6E). Some deformation bands, especially inside the footwall mixed zone and fault core, host calcite micro-veins located within their strongly comminute cores. These veins are arranged in two patterns: (1) fault-parallel geometry, which is the most frequent one and is characterized by veins with a maximum width of 800 µm; (2) tiny veins (maximum width <100 µm) arranged in left-stepping en-échelon array forming angles of 40–50° with slip surfaces, i.e., coherent geometry with extensional shearing.

In the fault core, foliated sandstone hosts thin black gouges consisting of a very fine-grained, dark-colored ultra-comminute matrix and a few survivor grains. Immediately outside the gouge layers, S-C type structures indicating extensional shear frequently occur (Fig. 6F). As observed at the meso-scale, and at the micro-scale, gouge layers show mutual cross-cut relationships with conjugate deformation band sets.

CEMENTATION PATTERN

Preferential cementation occurs throughout the investigated outcrop in the form of diagenetic concretions locally cementing the loose host sandstone. The vast majority of concretions are associated with deformation bands and faults. Bedding-parallel concretions are rare and usually show a limited lateral continuity and thickness typically lower than 5 cm (Fig. 3A). Inside the low-deformation domain, concretions hosted within faults and deformation bands display a tabular geometry with thickness varying between 5 and 10 cm, increasing in deformation band clusters and subsidiary faults. Almost all subsidiary faults and fault zones in the footwall damage zone are characterized by tightly cemented bodies (Fig. 3D). Here, concretions encase deformation bands and thick deformation band clusters to form cemented bodies as thick as 15–20 cm. The footwall mixed zone is characterized by an abrupt increase in concretion

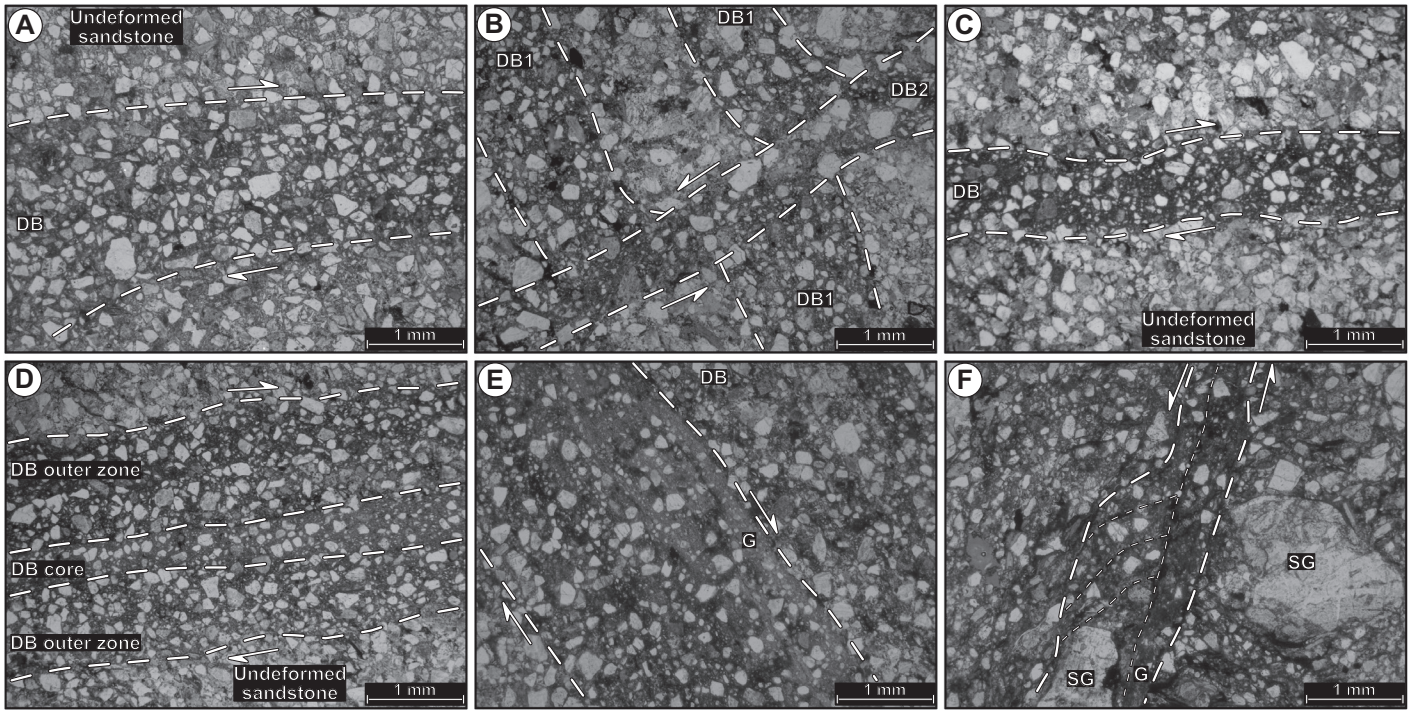

Figure 6. Petrographic characterization of different types of deformation elements sampled through the structural domains composing the Rocca di Neto fault zone. Deformation bands (DB) are hosted inside selectively cemented sandstone, while the black gouge is completely non-cemented. (A) Low-displacement DB in the low-deformation zone showing incipient fragmentation of grains. (B) Conjugate deformation bands (DB1 and DB2) within the footwall damage zone. (C) Fault-parallel, low-displacement DB inside the footwall damage zone. (D) Fault-parallel, high-displacement DB showing an ultra-comminute core and less deformed outer zone. (E) High-displacement DB with asymmetric gradient of grain size comminution and thin ultra-comminute gouge layer (G). (F) Black gouge layer (G) with extreme grain size reduction forming a fine-grained matrix surrounding a few survivor grains (SG). S-C structures are frequent inside foliated sand.

number and diagenetic bodies are offset along conjugate deformation band sets, thus showing limited thickness (<10 cm) and lateral continuity (Fig. 3D). The magnitude of the offset displayed by concretions is not constant throughout the entire structural domain, but depends on the accommodated displacement along the inclined conjugate system of deformation bands. Concretion development along the bounding surface of conjugate deformation bands resulted in geometric arrays resembling folds (Fig. 7). The intersections of the lineations between concretions with different dip, plot almost parallel to the strike of the master slip surface (Fig. 7). Inside the fault core, only one laterally continuous, 30–40-cm-thick tabular concretion occurs along the master slip surface.

Concretion Petrography

Cement petrography was investigated both on the undeformed as well as on the deformed sandstone inside deformation bands along the same concretions.

Concretionary bodies developed in undeformed loose sandstone of the low-deformation zone are made up of sparitic calcite with mosaic texture and crystal size up to 70–80 µm (C2 in Fig. 8A). The size of the crystals tends to increase where the pore space is larger. Locally, calcite cement forms also syntaxial overgrowths around peloids, fossil shells, and detrital calcite grains. Under cathodoluminescence (CL), this cement displays very bright yellow-orange luminescence, with a few and thin dull sub-zones (C2 in Fig. 8A). Concretions developed by preferential cementation along deformation bands and subsidiary faults within the low-deformation zone are characterized by cementation patterns similar to those developed in the undeformed sandstone, still with bright-yellow luminescence (C2 in Figs. 8D–8F). The main difference is the crystal size of calcite, which is typically <10–20 µm (Fig. 9A). Locally, grain boundaries have a 10-µm-thick fringe of undeformed equant calcite (Fig. 8D). Calcite cement, infilling intergranular pores, includes both crushed and undeformed calcite crystals, the latter still preserving the original shape (Fig. 9A). Intergranular pores are frequently partially filled by grain fragments and have very fine-grained sparitic calcite cement (Fig. 8F).

Concretions developed in undeformed sandstone within the footwall damage zone are characterized by a more complex cementation pattern. The dominant cement is still sparitic mosaic calcite, but with coarser size, up to 90–100 µm (Fig. 8B). Under CL, this calcite displays a dull dark-brown color in the core of the crystals (C1), followed by growth zonations with a bright-yellow luminescence (C2) (Fig. 8B). The observed CL-pattern varies according to the position inside concretions: concretion cores have a dominant dark-brown cement (C1), while moving to the outer edges bright-yellow sub-zones typically occur and eventually become the dominant cement type (C2) (Fig. 8B). Concretions developed along deformation bands within the footwall damage zone commonly encase a high number of closely spaced deformation bands. In these cases, deformation bands located close to concretion nuclei display very fine-grained calcite crystals (Fig. 9B) with brownish CL color (C1) (Fig. 8G). Deformation bands located in proximity of concretion outer edges are cemented by almost equal proportions of brown (C1) and yellow-luminescent fine-grained calcite (C2) (Fig. 8H).

Concretions developed in undeformed sandstone within the footwall mixed zone and fault core have a prevalent cement composed of sparitic calcite with crystal size ranging from 30 to 200 µm (Fig. 8C). Analysis under CL reveals dark-brown luminescence similar to the one characterizing cements from concretions sampled in the damage zone (C1) (Fig. 8B). However, no bright-yellow luminescent cement (C2) was found.

Concretions developed along deformation bands in the footwall mixed zone and fault core show again a dark-brown cement under CL (C1). In particular, deformed fine-grained cement is mixed with the fine matrix made up of crushed feldspar and to a lesser extent, quartz grains (Fig. 8I). Concretions encasing fault-parallel deformation bands show dark comminute cement inside cores, and less deformed, dark-brown calcite in the outer sectors (C1) (Figs. 8J and 9C).

Vein Petrography

Most of the veins pertaining to the fault-parallel pattern are partially cemented by mosaic equant to elongate (dogtooth) calcite (Figs. 8K and 9B), while only a few are completely filled. The CL color is brown dull-orange, similar to that shown by calcite cementing concretions outside the veins (C1 in Fig. 8K). En-échelon veins have a limited lateral continuity and are usually completely filled by mosaic calcite with brown CL color (Figs. 8L and 8M). Some of these veins display little drag and shearing in the vicinity of deformation bands.

Cement Stable Isotope Geochemistry

Stable isotope data acquired from concretions in different structural positions are reported in a $\delta^{18}O$-$\delta^{13}C$ cross-plot (Fig. 10A). In particular, concretions associated with deformation bands and subsidiary faults from the low-deformation zone, are characterized by $\delta^{13}C$ spanning in a wide range of values (from –23.08 to –8.98‰) and $\delta^{18}O$ with a narrow span (from –8.45 to –4.12‰ V-PDB). A concretion formed along an erosive surface not related to deformation structures has different isotopic signature, with less depleted $\delta^{13}C$ (from –9.3 to –0.08‰) and $\delta^{18}O$ (from –6.66 to –1.55‰ V-PDB) (Fig. 10A). Data from diagenetic bodies sampled inside the footwall damage zone show only a limited overlap with those from concretions in the low-deformation zone. In particular, $\delta^{13}C$ ranges from –10.35 to –0.02‰ while $\delta^{18}O$ values span from –5.39 to –1.25‰ V-PDB (Fig. 10A). Concretions within the footwall mixed zone have less depleted isotopic signatures, with $\delta^{13}C$ values spanning from –3.26 to –0.16‰ and $\delta^{18}O$ values in the –3.99 to –1.32‰ V-PDB range (Fig. 10A). Eventually, concretions sampled from the fault core have

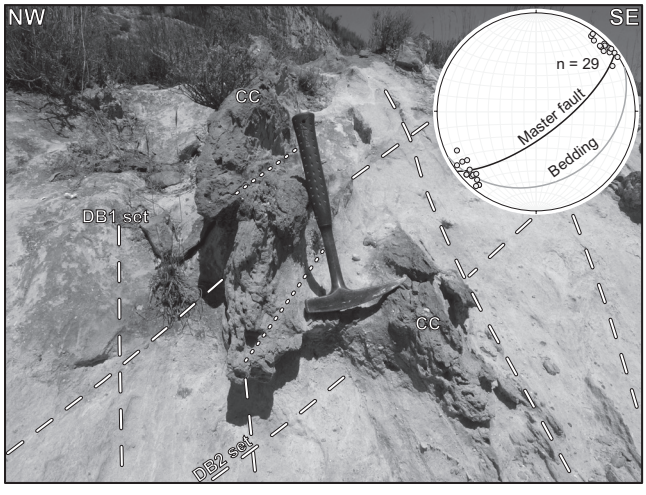

Figure 7. Outcrop photo of a concretion located within the footwall mixed zone, at a distance of 2 m from the master fault, resembling a folded-dragged geometry along the intersection line between the two conjugate deformation band sets. Poles in the stereonet are the intersection lines of the two conjugate sets of deformation bands. DB1—high-angle deformation band; DB2—low-angle deformation band; CC—carbonate concretion.

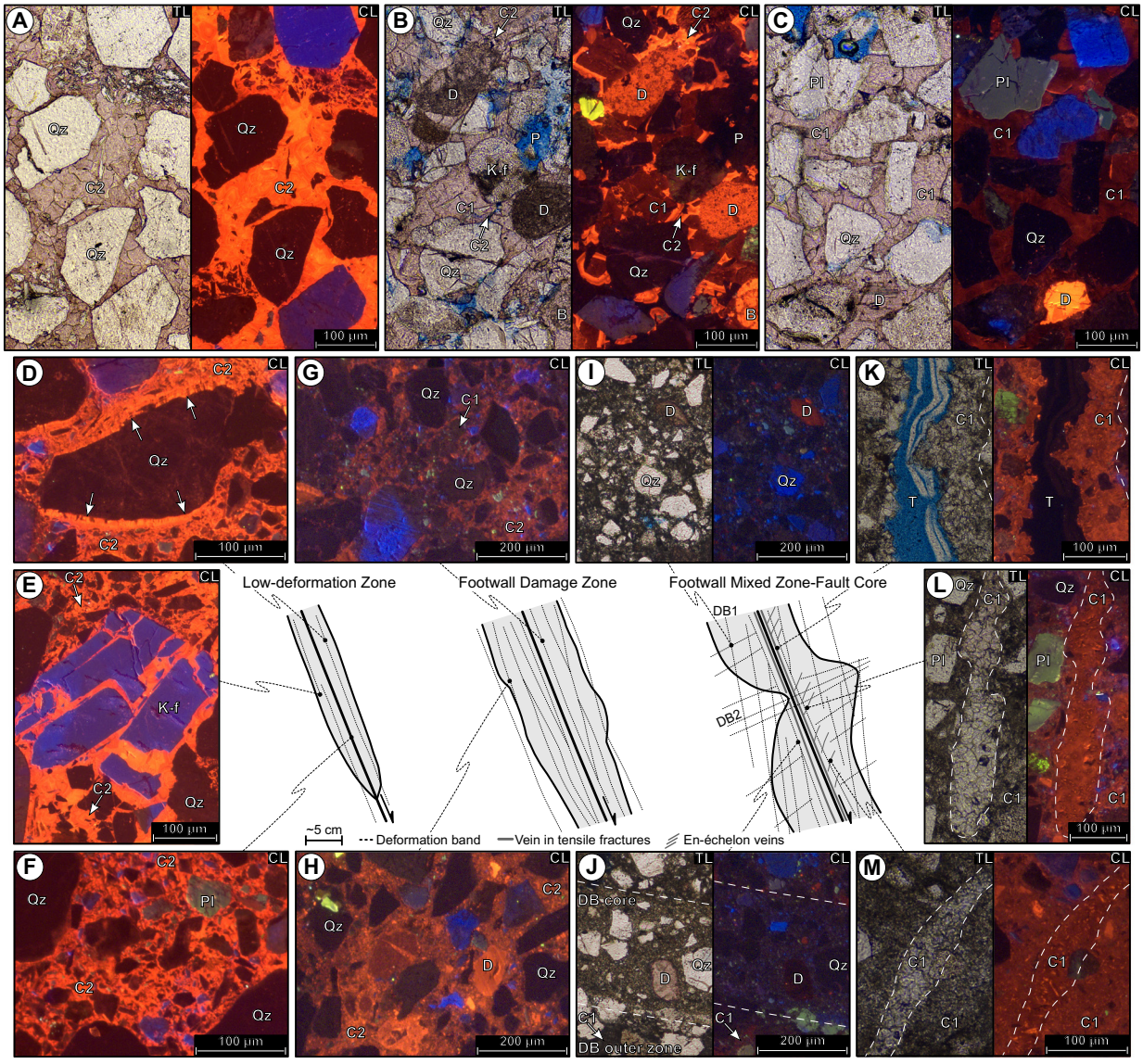

Figure 8. Petrographic photomicrographs of cement in the undeformed (A–C) and deformed (D–M) concretion volume. Pink color under transmitted light is due to the staining of carbonate cements obtained with a solution of alizarin red S, potassium ferricyanide, and hydrochloric acid. (A) Sparitic equant calcite with mosaic texture and yellow CL color (C2) inside concretion from the low-deformation zone. (B) Sparitic calcite with dark-brown luminescence (C1) enveloped by bright-yellow one (C2), characterizing concretion from the footwall damage zone. Note in the middle of the image the cracked brown-CL calcite crystal affected by micro-fractures filled by bright-CL cement. (C) Concretion along the fault core shows dull brown-colored coarse sparitic calcite (C1). (D) Fine-grained calcite cementing a deformation band located in the low-deformation zone. White arrows indicate a fringe of undeformed equant calcite along the outer rim of quartz grain. (E) Detail of calcite cementing a fractured feldspar grain within a band inside the low-deformation zone: cement is coarser where pore space is wider. (F) Core of a band inside the low-deformation zone displaying finely grained sparitic calcite. (G) Dully luminescent crushed calcite (C1) inside a deformation band close to the core of a concretion hosted in the footwall damage zone. (H) Crushed bright-orange cement (C2) found in a deformation band along the outer edge of a concretion within the footwall damage zone. (I) Conjugate deformation bands showing low amount of dull-brown crushed cement (C1) within concretion from the footwall mixed zone. (J) Fault-parallel high-displacement band inside the footwall mixed zone with heavily crushed dull syn-kinematic cement (C1) both in the core and in the outer zone of the band. (K) Fault-parallel tensile fracture developed within concretion from the footwall mixed zone, with partial infilling. (L) Vein composing the en-échelon array, filled by equant mosaic calcite. (M) En-échelon vein slightly sheared within a concretion from the fault core. Qz—quartz; K-f—feldspar; Pl—plagioclase; D—detrital calcite; B—bioclast; P—pore; DB—fault-parallel deformation band; DB1—high-angle deformation band; DB2—low-angle deformation band; T—tensile fracture; C1—dull-CL calcite cement; C2—bright-CL calcite cement; TL—transmitted light; CL—cathodoluminescence.

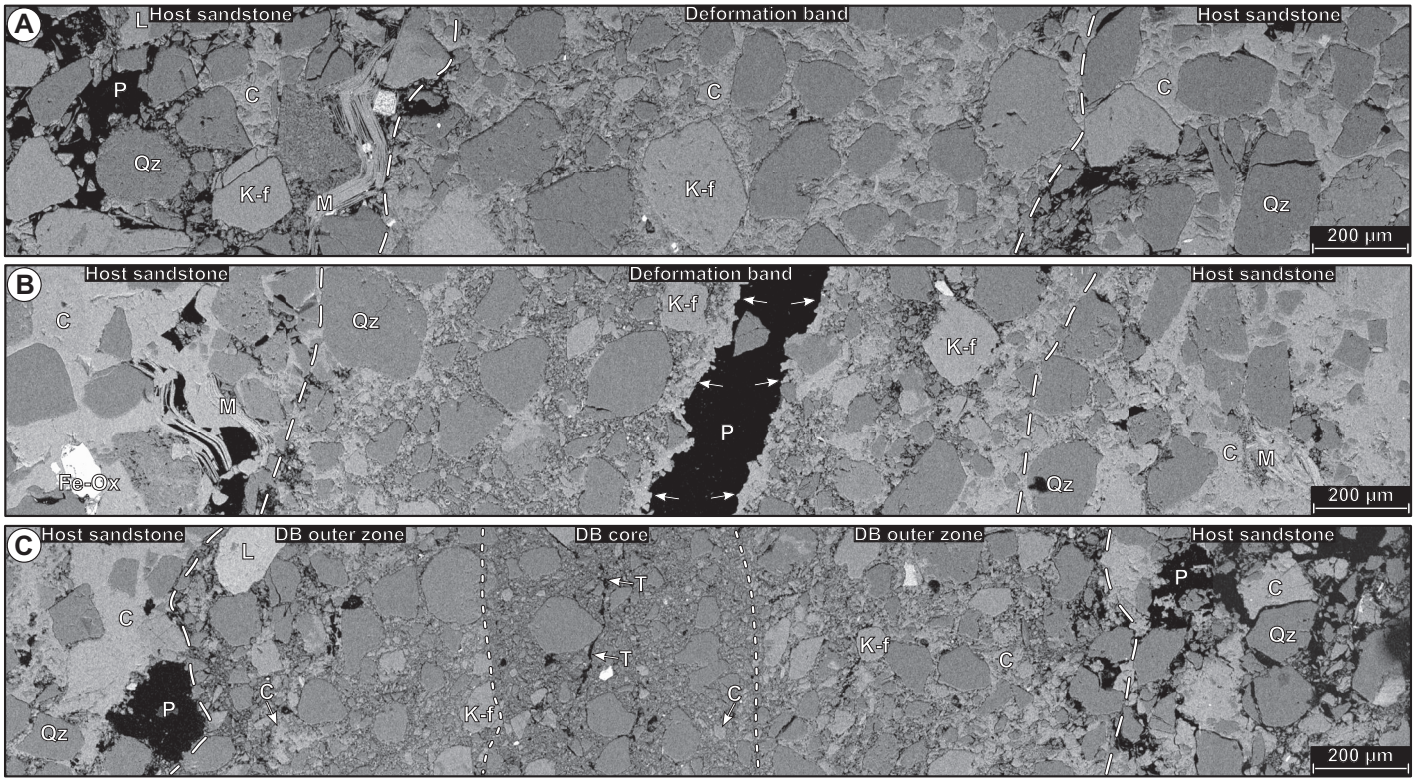

Figure 9. Backscattered scanning electron microscope photomicrographs of representative deformation bands sampled from the structural domains forming the Rocca di Neto fault zone. (A) Band with low-displacement within the low-deformation zone, cemented by a coarse equant calcite outside and fine-grained one inside band boundary. (B) Medium-displacement deformation band from the footwall damage zone showing the same cement pattern, with a tensile fracture in the middle partially filled by cement (white arrows). (C) High-displacement deformation band close to the main fault with almost no cement in the core zone, while it is sparsely distributed in the outer zone of the band. A tiny tensile fracture developed in the middle of the core of the band. Qz—quartz; K-f—feldspar; M—mica; C—calcite; L—lithic fragment; Fe-Ox—iron oxide; P—pore; T—tensile fracture; DB—deformation band.

isotopic values of $\delta^{13}C$ spanning from –8.09 to –0.49‰, while $\delta^{18}O$ values vary from –7.51 to –2.09‰ V-PDB (Fig. 10A).

Data from sampling transects along and across concretions show peculiar isotopic signatures. Concretions from the low-deformation zone are characterized by the most depleted $\delta^{13}C$ values (–20.18‰) located in the central parts of the cemented cores, while outer edges have less depleted isotopic signatures (–13.31‰) (Fig. 10B). $\delta^{18}O$ values describe asymmetrical variations, being the most depleted sector located close to one boundary (–6.71‰ V-PDB), whereas less depleted signatures characterize concretion cores (around –5.51‰ V-PDB) and least depleted values occur close to the other boundary (–4.56‰ V-PDB) (Fig. 10B). Concretions from the footwall damage zone show symmetric variations in isotopic values with respect to their geometry. The most depleted $\delta^{13}C$ values (–10.35‰) are recorded along the outer zones, while cores have the least depleted values (–2.34‰) (Fig. 10C). $\delta^{18}O$ data follow the same trend described by carbon, with the most depleted values close to cores (–5.39‰ V-PDB) and the least depleted ones pertaining to the outer edges (–2.92‰ V-PDB) (Fig. 10C). The concretion from the fault core displays more stable isotopic signatures along the two trends in comparison with data from the footwall damage zone. From the core to the outer edge, $\delta^{13}C$ values display a variability between –1.89 and –0.9‰, whereas $\delta^{18}O$ values span from –4.03 to –2.2‰ V-PDB (Fig. 10D). However, considering all concretion samples from the fault core there is a significant isotopic variability from one sample to the other.

UNIAXIAL COMPRESSION STRENGTH DATA

Undeformed and loose pristine host sandstone is characterized by Schmidt hammer rebound values lower than the detection limit of the instrument (8.5 Q) (Fig. 11). Within the footwall damage zone, deformation bands pertaining to DB1 set are characterized by a mean Q value of 12.03, while deformation bands pertaining to DB2 set have a mean value of 11.43 (Fig. 11). Fault-parallel deformation bands (DB) hosted within the footwall mixed zone are characterized by a mean Q value of 13.7. A tabular concretion cementing a low-displacement fault in the low-deformation zone displays a mean Q value of 50.13, while inside the footwall damage zone a similar body has a mean Q value of 61.7. Deformed concretions in the footwall mixed zone and fault core have mean rebound values of 58.06 and 35.76, respectively (Fig. 11). Collectively, diagenetic concretions have mean Q rebound values 3–5 times higher than uncemented deformation bands.

DISCUSSION

Regional and Kinematically Induced Stress Fields from Conjugate Deformation Bands

The investigated fault zone has peculiar striking deformation patterns considering the low-deformation zone and the fault zone itself (damage zone, mixed zone, and fault core).

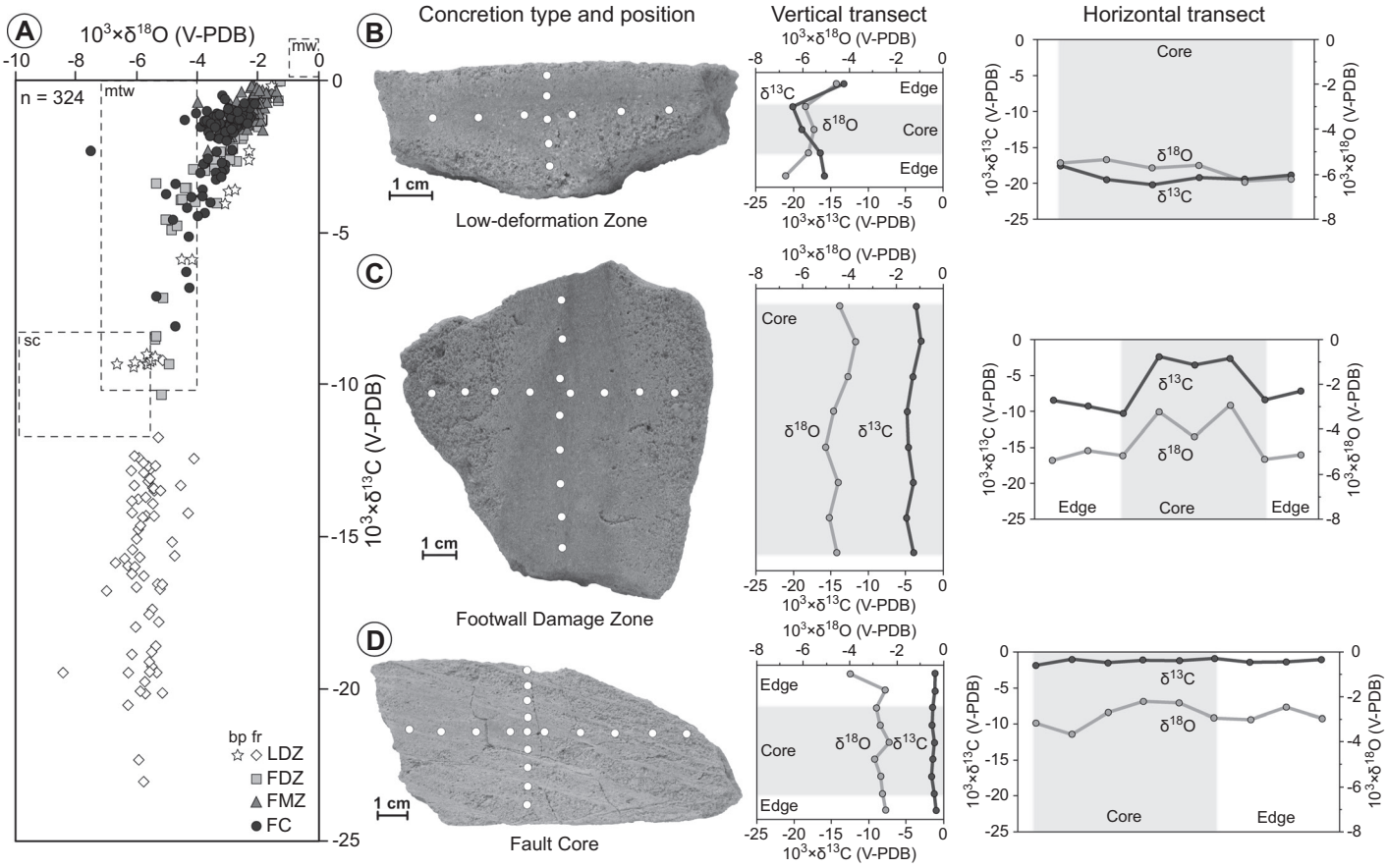

Figure 10. Stable isotope data extracted from concretionary bodies sampled throughout the Rocca di Neto fault zone. (A) $\delta^{18}O$-$\delta^{13}C$ cross-plot of the cumulative data gained from all sampled concretions. (B) Concretion sampled in the low-deformation zone displays the most depleted $\delta^{18}O$ and $\delta^{13}C$ values. (C) Concretion sampled within the footwall damage zone shows least depleted isotopic response close to the core, while the outer edge has the more depleted ones. (D) Concretion from fault core has roughly constant and scarcely depleted $\delta^{18}O$ and $\delta^{13}C$ isotopic signature. LDZ—low-deformation zone; FDZ—footwall damage zone; FMZ—footwall mixed zone; FC—fault core; V-PDB—Vienna Pee Dee belemnite; fr—fault-related concretion; bp—bedding-parallel concretion; mw—marine water cement; mtw—meteoric water cement; sc—soil-derived cement.

By applying basic fault mechanics (e.g., Mandl, 2000), conjugate deformation bands offer the possibility to determine the orientation of the principal axes of the stress ellipsoid both inside and outside the Rocca di Neto footwall damage zone (Figs. 2C and 12). In the low-deformation domain, outside the fault zone, the intersection line between DB1 and DB2 deformation band sets yields the orientation 234°, 4° (strike-dip) for the σ_2 axis. The bisector of the angle between the two conjugate sets yields a σ_1 oriented almost vertically, with a slight plunge toward the north (8°, 86°). The pole of the σ_1-σ_2 plane provides the orientation of σ_3 (145°, 3°), which is consistent with the extension direction inferred from slickenlines (Fig. 12A). In the footwall damage zone, mixed zone, and fault core the bisector of the average angle between the two DB1 and DB2 conjugate deformation band sets provides a NW-plunging σ_1 axis (306°, 65°), describing an angle of 44° with the trace of the master slip surface. The intersection line between DB1 and DB2 yields an almost horizontal σ_2 axis, with a slight plunge toward NE (45°, 3°). The pole of the σ_1-σ_2 plane provides the orientation of the σ_3 axis (137°, 25°) (Fig. 12B).

Results from inversion of deformation band data indicate that: (*i*) two different paleo-stress fields occurred in the study area, outside and inside the footwall damage zone of the Rocca di Neto fault, respectively; (*ii*) the paleo-stress field inferred from the low-deformation zone is typical of "Andersonian extensional faulting" (i.e., bisecting the acute dihedral angle (48°) described by conjugate deformation bands. Following this, σ_1 plots at 24° from deformation band surfaces and is almost vertical; e.g., Mandl, 2000) (Fig. 12A). This can be assumed to represent the regional (basin-scale) stress field affecting the Crotone Basin since Middle Pleistocene times (Zecchin et al., 2012), because the orientation of the principal axes of the stress ellipsoid fits well with the mean NE-SW trend of extensional fault zones involving Pleistocene sediments; this regional stress field could be associated both to the tectonic uplift as well as to the pull-apart structure formed between the bounding shear zones (Van Dijk, 1994; Ferranti et al., 2009; Zecchin et al., 2012) (Fig. 1B). (*iii*) The paleo-stress field inferred from the footwall damage zone and mixed zone is not compliant with the classic "Andersonian faulting," rather the inclination of σ_1 with respect to the master slip surface fits extremely well with a kinematically induced stress field (e.g., Davis et al., 2012) produced by fault activity in a 8–10-m-wide belt from the master slip surface (Fig. 12B). σ_1 bisects the acute dihedral angle (59°) and plots at 44° from the master fault trace (Fig. 12B). In this view, conjugate high- and low-angle deformation band sets can be interpreted as Riedel shears (Petit, 1987; Davis et al., 2000; Ahlgren, 2001; Katz et al., 2004; Olsson et al., 2004). In particular,

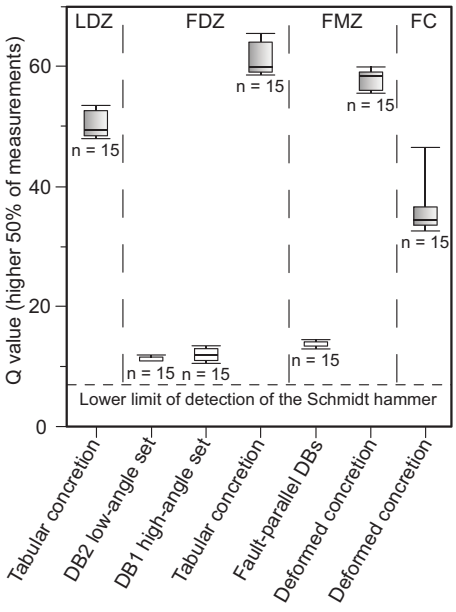

Figure 11. Schmidt hammer rock relative strength (Q value) measurements for different types of deformation bands and diagenetic bodies along the Rocca di Neto fault zone. DB—deformation band; DB1—high-angle deformation band; DB2—low-angle deformation band; LDZ—low-deformation zone; FDZ—footwall damage zone; FMZ—footwall mixed zone; FC—fault core.

DB1 deformation band set constitutes synthetic R shears (at ~17° to the master slip surface), while DB2 features antithetic R^1 shears (at ~74° to the master slip surface) (Davis et al., 2000). The orientation of the σ_1 axis of the kinematically induced stress field with respect to the master slip surface, as well as that of R and R^1 shears, indicates that slip on the master fault itself occurred by simple shear.

Deformation Mechanisms and Physical Strain-Hardening

Deformation in the Rocca di Neto fault zone occurred at very shallow burial depth (<1 km) (Balsamo and Storti, 2010; Zecchin et al., 2012). This hypothesis is further supported by the limited thickness of the stratigraphic succession overlying the formations involved in deformation along the fault zone and by the limited compaction and high-porosity characterizing the pristine sandstone (Balsamo and Storti, 2010; Zecchin et al., 2012). The deformation mechanisms responsible for the development of deformation bands and gouges are particulate flow followed by cataclasis. In particular, outside the footwall damage zone, non-destructive particulate flow (Rawling and Goodwin, 2003) was the dominant deformation mechanism active during deformation band formation, witnessed by grain reorganization with negligible sliding and limited fragmentation (Fig. 6A). However, evidence of cataclasis are found only inside thick clusters of deformation bands or along subsidiary faults (Fig. 13A). Conversely, cataclasis and wear processes (e.g., Engelder, 1974; Rawling and Goodwin, 2003; Balsamo and Storti, 2010, 2011) occurred extensively in the footwall damage zone, where they overprinted early particulate flow, as indicated by the severe fragmentation and comminution affecting the grains (Figs. 6B–6F). The switch between the two deformation mechanisms was likely facilitated by: (1) significant loss of sediment porosity by tectonic compaction within the fault zone promoting a tighter fabric and increasing grain to grain contacts (Antonellini et al., 1994; Shipton et al., 2005); (2) early selective cementation localized along deformation bands and faults (Mozley and Goodwin, 1995; Caine and Minor, 2009; Philit et al., 2015; Skurtveit et al., 2015; Williams et al., 2017); (3) increase of fault displacement locally accommodated within deformation bands (Torabi et al., 2007; Kaproth et al., 2010); (4) increasing strain near the master slip surface (Cashman and Cashman, 2000; Mair et al., 2000). There is a displacement gradient moving to the master fault, so that deformation structures found close to it, typically display a more mature cataclastic fabric following higher displacement magnitude.

The strain-hardening behavior of deformation mechanisms in the fault zone (Aydin and Johnson, 1978; Mair et al., 2000; Fossen et al., 2018) is supported by the abrupt increase of deformation band density occurring in the footwall damage zone, mixed zone, and fault core (Fig. 4). The presence of ultra-comminute layers in the central cores of deformation bands (Figs. 6D, 6E, and 13B) and micro-veins developed within these layers, provides evidence for late-stage shear and strain-localization processes of deformed sandstone (Aydin and Johnson, 1978; Davatzes et al., 2005; Fossen et al., 2018) that eventually is suitable to fail by Coulomb shear due to the increased cohesion (Fossen, 2010; Davis et al., 2012) (Fig. 13C). The slightly positive trend of Q values moving from deformation bands in the outer part of the footwall damage zone toward the mixed zone (Fig. 11) is associated with the corresponding increase of comminution intensity due to higher displacement along single bands. The late-stage localization of deformation could be due to transient strain-softening behavior of deformation bands reached just before the yield point, facilitating the slip accommodation (Mair et al., 2000). Another possible explanation could be the overcome of frictional properties of the cemented and deformed sandstone operated by the stress conditions imparted by the master fault (syn-kinematic stress field).

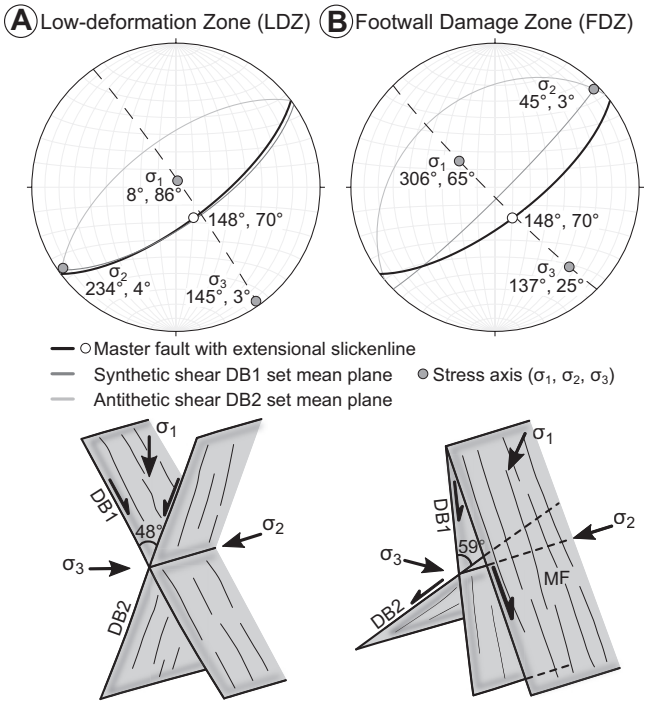

Figure 12. Orientation of stress field deduced from conjugate deformation bands found in the low-deformation zone and within the footwall damage zone, based on geometrical relationships shown in Figure 5 (Schmidt lower hemisphere projection). (A) Stress field inferred from conjugate deformation band sets inside the low-deformation zone. (B) Stress field inferred from inclined conjugate deformation band sets inside the footwall damage zone. DB1—high-angle deformation band; DB2—low-angle deformation band; MF—master fault.

Syn-Kinematic Cementation and Chemical Strain-Hardening

Selective cementation in the form of carbonate concretions is strictly linked to deformation structures (deformation bands, clusters of bands, and subsidiary faults), while bedding-related concretions are only a few and limited to the

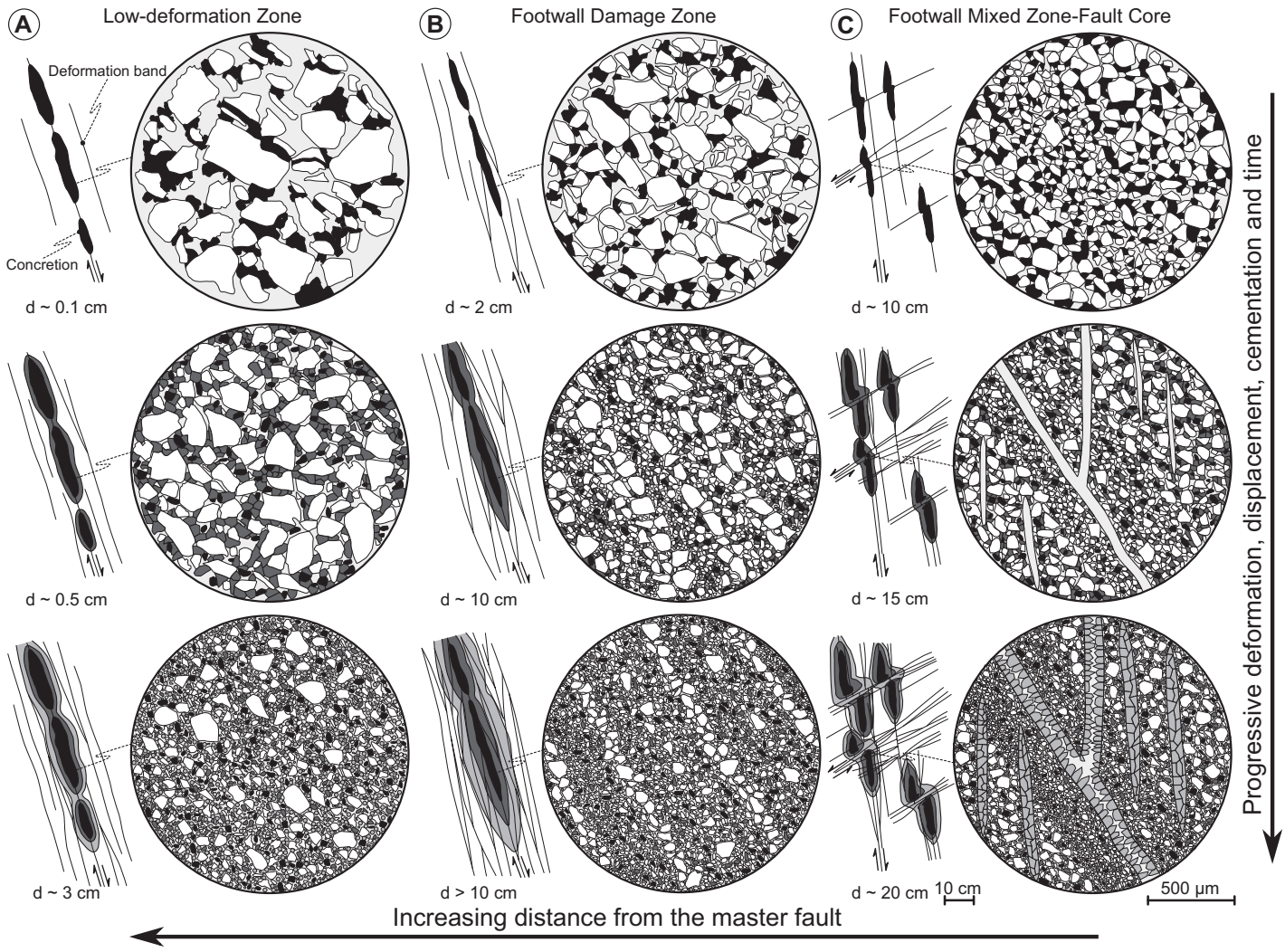

Figure 13. Schematic evolution of microstructures and syn-kinematic cementation in different structural domains along the Rocca di Neto fault zone. (A) Progressive cementation and deformation characterizing arrays of fault-parallel deformation bands to form tabular-shaped concretionary bodies inside the low-deformation zone. (B) Syn-kinematic cementation of dense cluster of deformation bands within the footwall damage zone. The resulting concretion is typically thicker compared to the ones characterizing the low-deformation zone. (C) Cementation coeval with deformation along the conjugate deformation band sets inside the footwall mixed zone and fault core, close to the master fault. The shape of the resulting concretions features "folded-dragged" geometry given by the intersection and mutual cross-cut relationship between the two deformation band sets. Note the micro-veins, both parallel and with en-échelon pattern characterizing these concretions, as a result of both chemical and physical strain-hardening achieved in the nearest vicinity of the master fault. d—displacement.

low-deformation domain. Cement started to form within deformation bands and subsidiary faults possibly enhanced by the presence of crushed detrital fossil shell fragments acting as cementation nuclei for successive calcite precipitation (Bjørkum and Walderhaug, 1990). In addition to the role of calcite fragments in favoring cementation, also crushing and pervasive fracturing of siliciclastic grains could have facilitated the continuous cementation (Williams et al., 2015). The lower porosity and permeability within faulted sediments could have caused an increase of fluid retention time regardless of the water-saturation conditions, leading to a continuous cementation through time (Antonellini et al., 1994; Sigda and Wilson, 2003; Wilson et al., 2003). Moreover, the presence of black thin gouges in the fault core supports coseismic slip events (Balsamo and Storti, 2011; Balsamo et al., 2014), which might have caused rapid drops of CO_2 pressure, inducing fast calcite precipitation within deformation bands located close to the master fault (Hendry and Poulsom, 2006).

The isotopic signature of cements recorded different fluid nature during calcite precipitation in different fault sectors. The marine water end-member was assumed from mollusk shells sampled from other nearby faults by Balsamo et al. (2012) and is characterized by a mean $\delta^{13}C$ of + 0.3‰ and a $\delta^{18}O$ of –0.5‰ V-PDB.

To directly compare the isotopic data sets from different structural positions of the fault zone, the $\delta^{18}O$ isotopic composition of the parental fluids was back-calculated. To this end, we adopted the fractionation formula of Friedman and O'Neil (1977), assuming 10 °C as the temperature of superficial fluids, 500 m as the maximum burial depth and a geothermal gradient of 20 °C/km. Data were compared with the expected $\delta^{18}O$ of meteoric fluids characterizing the Crotone Basin (Giustini et al., 2016). According to this, the $\delta^{18}O$ of marine water reported in a previous work

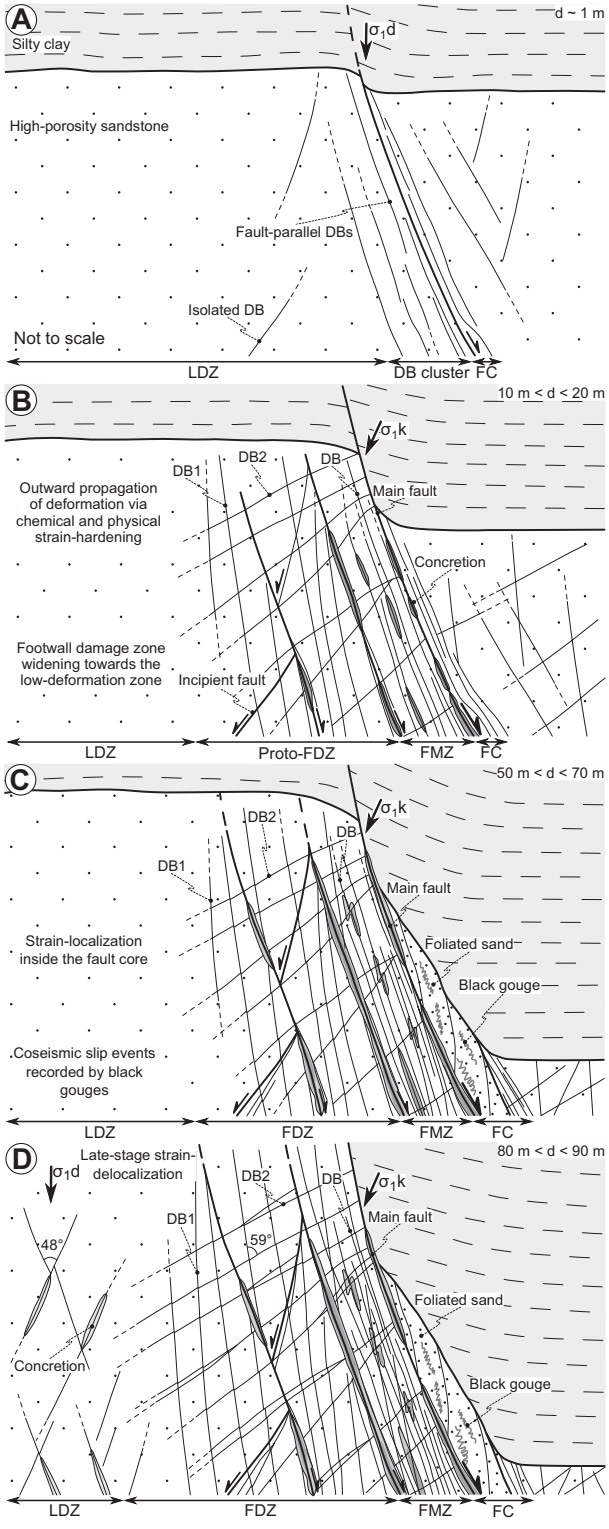

Figure 14. Evolutionary model of the studied Rocca di Neto fault zone. (A) Early stage of deformation with nucleation of deformation bands in a marine pore water-dominated diagenetic environment. At this stage the fault zone consisted of a cluster of deformation bands formed under the regional-dynamic stress field. (B) With progressive displacement the fault zone widened toward the undeformed domain due to the tectonic compaction and preferential cementation occurring under mixed marine-meteoric pore fluids. The conjugate deformation bands formed under a kinematic stress field produced by the displacement accommodation along the fault core. During this stage the footwall mixed zone and damage zone formed, the latter hosting conjugate deformation bands and subsidiary faults. (C) With continuing strain accommodation the fault zone reached a critical width that forced the localization of the deformation along the fault core. Displacement was likely accommodated by alternating coseismic and slow slip events affecting tectonically compacted sandstone, producing black gouges and deformation bands inside the fault core. At the same time, inside the footwall damage zone the conjugate deformation bands underwent clustering and contributed to the overall displacement partitioning. Some concretions were deformed along the deformation bands and recorded an isotopic signature shifting progressively from mixed marine-meteoric to meteoric fluids. (D) In the last stage of uplift the deformation is delocalized toward the low-deformation zone, where widely spaced conjugate bands formed. Concretions hosted along these deformation bands and subsidiary faults are characterized by marked meteoric signature. LDZ—low-deformation zone; FDZ—footwall damage zone; FMZ—footwall mixed zone; FC—fault core; DB—fault-parallel deformation band; DB1—high-angle deformation band; DB2—low-angle deformation band; σ_{1d}—dynamic maximum stress axis; σ_{1k}—kinematic maximum stress axis; d—displacement.

(Balsamo et al., 2012) results + 0.5‰ V-SMOW, while present day meteoric fluids in the Crotone Basin have an isotopic signature spanning from –7 to –5‰ V-SMOW (Giustini et al., 2016). (For further details on back-calculation of $\delta^{18}O$ of parental fluids, see Data Repository Table DR4; see footnote 1.)

The $\delta^{18}O$ of parental fluids from the fault core samples displays a pronounced span with data ranging from –6.51 to –1.08‰ V-SMOW. Together with the range of $\delta^{13}C$ (–8.09 to –0.49‰ V-PDB), this suggests a mixed source of fluids, with the less depleted values corresponding to mixed marine-meteoric fluids and the more depleted to meteoric ones (Hudson, 1977; Giustini et al., 2016) (Figs. 10A and 10D). This is further supported by the dull-brown CL-response of cements and veins (C1), suggesting oxidizing conditions (Barnaby and Rimstidt, 1989) (Figs. 8C and 8K). Concretions from the footwall mixed zone have a narrower interval of $\delta^{18}O$ values with respect to the ones from the fault core (–2.63 to –0.32‰ V-SMOW). These values would suggest again a mixing of marine and meteoric water, with the first one being the dominant component, as further indicated by the $\delta^{13}C$ oscillating between –3.26 and –0.16‰ V-PDB (Hudson, 1977; Giustini et al., 2016) (Fig. 10A). C1 calcite with brown-dull CL response supports oxidizing conditions during precipitation (Barnaby and Rimstidt, 1989). The footwall damage zone hosts concretions formed by fluids with $\delta^{18}O$ spanning from –4.38 to –0.24‰ V-SMOW. $\delta^{13}C$ describes a large span from –10.35 to –0.02‰ V-PDB, thus suggesting an evolving fluid source from marine to meteoric during progressive cementation (Hudson, 1977; Giustini et al., 2016) (Figs. 10A and 10C). The spatial distribution of C1 and C2 cements along concretionary bodies (from the edge to the nucleus) indicates that the first cement is related to pore fluids with mixed marine-meteoric isotopic signature, while the second one to meteoric pore fluids (Fig. 8B). The change from brown-dull to bright luminescence could be related to the onset of more reducing conditions during cementation (Barnaby and Rimstidt, 1989) (Figs. 8B, 8G, and 8H). Eventually, concretions from the low-deformation zone were formed by fluids with $\delta^{18}O$ from –7.44 to –0.54‰ V-SMOW and with $\delta^{13}C$ spanning from –23.08 to –0.08‰ V-PDB (Figs. 10A and 10B). However, it has to be stressed that these considerably wide ranges of variation are due to the inclusion of one bedding-related concretion inside the data set. In fact, fault-related concretions have $\delta^{18}O$ of parental fluids spanning from –7.44 to –3.11‰ V-SMOW, with a $\delta^{13}C$ ranging from –23.08 to –9.2‰ V-PDB (Fig. 10A). On the contrary, bedding-related concretion has $\delta^{18}O$

values from –5.65 to –0.54‰ V-SMOW and $\delta^{13}C$ from –9.39 to –0.08‰ V-PDB (Fig. 10A). According to these data, fault-related concretions in the low-deformation zone formed under meteoric fluid circulation, with contribution from percolation through soils and bacterial-mediated alteration of organic matter (Hudson, 1977; Nelson and Smith, 1996) (Figs. 10A and 10B). The bedding-related concretion nucleated under mixed marine-meteoric conditions, while the last cementation stages involved markedly meteoric fluids. Bright CL-response shown by these concretions further supports the hypothesis of a meteoric origin of pore fluids and reducing conditions produced by fermentation of organic matter (Barnaby and Rimstidt, 1989) (Figs. 8A, 8D, and 8E). Since the bedding-related concretion is not constrained to deforming structures it recorded a complete diagenetic history imparted by mixed marine-meteoric fluids in the early diagenesis stage and by markedly meteoric fluids in the last cementation phase (see Data Repository Table DR3 for statistical analysis on isotopic data sets; see footnote 1).

The presence of both undeformed and crushed fine-grained cement inside deformation bands, as well as slickenlines formed by mechanical striations, suggests that partial cementation started during deformation (syn-kinematic) and was then completed by younger, undeformed cement (post-kinematic) (Figs. 8D–8H). In high-displacement deformation bands close to the fault core, the very limited free pore volume due to strong tectonic compaction, prevented the extensive early stage cementation (Skurtveit et al., 2015) (Figs. 8I and 8J).

Development of syn-kinematic carbonate concretions along two cross-cutting orientations progressively created a network of much stronger material compared to cohesive deformation bands (see Fig. 11). Accordingly, the overall strength of the footwall damage zone likely increased through time. Moreover, the presence of a dense network of cohesive material within poorly lithified sandstone triggered a complex pattern of stress concentration patterns, facilitating brittle failure as highlighted by the striations, micro-fractures, and veins shown by concretions located close to the master fault (Figs. 8K–L). Striations are found only upon concretions and deformation bands due to the higher cohesion with respect to the tectonically compacted surrounding sandstone.

Fault Zone Evolution

The multidisciplinary data set collected in the structural domains composing the Rocca di Neto extensional fault zone, allowed us to obtain robust constraints on its structural evolution, framed within varying diagenetic environmental conditions. Deformation in the Scandale sandstone, which was deposited following a regional subsidence pulse (Zecchin et al., 2012), likely started in a marine pore fluid-dominated environment and very shallow burial of ~400–500 m, on the basis of stratigraphic constraints (Balsamo and Storti, 2010; Zecchin et al., 2012). The extensional shear zone originated as a fault-parallel deformation band cluster, developed in response to a basin-scale vertical σ_1 (Fig. 14A), similar to what is described in many other extensional settings worldwide (Aydin and Johnson, 1978; Shipton and Cowie, 2003; Ballas et al., 2015; Soliva et al., 2016) and in other fault zones affecting the high-porosity sandstones of the Crotone Basin (Balsamo and Storti, 2010, 2011). At this stage, the fault core consists of a few cm thick slip surface on one side of the deformation band cluster (Fig. 14A). No concretions with clear marine isotopic signature were found in the studied exposures of the Rocca di Neto fault zone, thus suggesting that early structural diagenesis did not include selective cementation of deformation bands. This feature may relate to under-saturated conditions of marine water with respect to carbonate species (Bjørkum and Walderhaug, 1990).

The well-known strain-hardening behavior of deformation bands (e.g., Aydin and Johnson, 1978; Mair et al., 2000; Fossen et al., 2018) caused progressive widening of the shear zone by outward migration of deformation, producing new fault-parallel deformation bands and a proto-damage zone during regional uplift and transition from a marine-dominated environment to a mixing zone of marine and meteoric fluids (Fig. 14B). This inference is based on the isotopic signature of tabular to lens-shaped concretions that started to nucleate along deformation bands, deformation band clusters, and faults likely due to capillary suction and to high retention time of fluids inside faulted sandstone (Sigda et al., 1999; Sigda and Wilson, 2003; Wilson et al., 2003; Balsamo et al., 2012). The footwall mixed zone nucleated next to the narrow fault core almost coevally with the proto-damage zone, and cementation started along deforming structures inside these domains (Fig. 14B). This is further confirmed by the isotopic signature shown by concretions close to the master fault, which suggests cementation operated by fluids with composition close to the marine water end-member (Figs. 10C and 10D). The combination of tectonic compaction (Engelder, 1974; Mair et al., 2000; Kaproth et al., 2010; Fossen et al., 2018) and preferential cementation (Mozley and Goodwin, 1995; Caine and Minor, 2009; Balsamo et al., 2012) with continuing fault slip, further enhanced the overall strain-hardening behavior within the fault zone, which continued propagating outward into the undeformed sediments. Under the new kinematically induced stress field, dense clusters of fault-parallel deformation bands progressively developed around pre-existing faults as well as inclined conjugate sets (Fig. 14B).

Eventually, the fault zone reached a critical width and a threshold value of overall strength, deformation delocalization ceased, and further slip was accommodated inside the fault core and along the master fault (Fig. 14C). This switch to localization of deformation could be related to the overcoming of frictional properties of deformed sandstone by the kinematic stress field induced by accommodation of displacement along the master fault, or to transient strain-softening behavior inside the fault core. According to isotopic data from concretions, this happened when fluids circulating within the Scandale sandstone were located in the mixing zone between marine and meteoric water. Further evidence supporting the localization of deformation in the fault core are provided by diagenetic bodies hosted close to the master fault, which recorded isotopic signature more depleted than the footwall mixed zone and more similar to the one characterizing concretions in the footwall damage zone.

In the fault core, thin layers of black gouge formed, indicating occurrence of coseismic events (Balsamo et al., 2014). Seismic activity supports further increase of fault strength and this provides a mechanical explanation for the formation of conjugate R and R^1 shears (Davis et al., 2000; Ahlgren, 2001; Katz et al., 2004) at this stage, as a consequence of greater rock strength overcome by the kinematically induced stress field within the fault zone. Development of R and R^1 shears might have helped in partitioning coseismic as well as interseismic slip. Isotopic signature of concretions formed along DB1 and DB2 deformation band sets, indicates ongoing cementation and faulting in a diagenetic environment progressively shifting from mixed marine-meteoric pore fluids toward markedly meteoric fluids (Figs. 10A and 10C).

Concomitant formation of DB1 and DB2 deformation band clusters overprinting the previously formed fault-parallel DBs, and preferential cementation along them during the last stage of uplift, eventually resulting in a complex network of intersecting, strain-hardening structures that progressively hampered the prosecution of deformation within the fault zone. Residual deformation was accommodated inside the low-deformation zone outside the fault zone during the last stage of strain delocalization (Fig. 14D). This process occurred at extremely shallow depth and lower confining pressure, as indicated by (*i*) the

narrower conjugate angles between deformation bands and faults (Mair et al., 2002), (*ii*) the particulate flow and more immature cataclastic fabric, and (*iii*) the isotopic signature of the corresponding syn-kinematic concretions, which indicates shallow meteoric fluid conditions with a possible contribution from plant-related organic matter fermentation inside soils (Hudson, 1977; O'Leary, 1981; Nelson and Smith, 1996) (Fig. 10A).

CONCLUSIONS

We described the deformation architecture and the structural-diagenetic evolution of the Rocca di Neto fault, a complex extensional fault zone affecting poorly lithified, high-porosity sediments in the Crotone Basin, Southern Apennines. The fault zone shows widespread evidence of deformation characterizing high-porosity sandstones (deformation bands and gouges) and preferential cementation (carbonate concretions), which concurrently occurred during fault slip. Major results from the combination of field measurements, microstructural, petrographic, diagenetic, and isotopic data can be summarized in the following points.

(1) Particulate flow and cataclasis were the dominant deformation mechanisms. The first one was active during the early stages of deformation, while with increasing burial and fault displacement, cataclasis became dominant in narrow slip zones and black gouges. The switch between the two mechanisms was favored by the porosity loss induced by tectonic compaction, little burial, and selective cementation.

(2) Concretions developed during fault activity, recording the shift from several diagenetic environments during the uplift history of the fault zone. Oldest concretions are located along the fault core and footwall mixed zone and record mixed marine and meteoric isotopic signatures. Through the footwall damage zone, concretions become progressively younger and are characterized by isotopic data shifting from mixed marine-meteoric to meteoric fluids. Outside the footwall damage zone, isotopic data show a marked meteoric signature, with contribution from fluids interacting with soils and organic matter alteration. Considering the continuing tectonic uplift affecting the investigated portion of the Crotone Basin, this condition was reached in the late stage of deformation, therefore concretions hosted in the low-deformation zone are the most recent diagenetic bodies occurring along the fault zone.

(3) Physical (tectonic compaction) and chemical (selective cementation) strain-hardening processes caused initial delocalization and outward propagation of deformation, followed by localization and onset of deformation triggered by the kinematically induced stress field along the master fault. Eventually, strain-hardening hampered further significant accommodation of deformation within the footwall damage zone and favored late-stage delocalization of low-displacement deformation banding and faulting in the low-deformation zone.

(4) Occurrence of a simple shear-related deformation fabric overprinting fault-parallel deformation bands and deformation band clusters, suggests that physical (and possibly chemical) strain-hardening is necessary to eventually increase the magnitude of the kinematically induced stress field, up to values overcoming the yield strength of the tectonically compacted, poorly lithified sediments. Such a stress magnitude increase might have been favored by the onset of episodic coseismic activity along the master fault.

(5) The overall deformation pattern suggests that activity of the Rocca di Neto fault zone occurred by aseismic creep and possibly slow slip (deformation bands), episodically overprinted by seismic slip (black gouges).

ACKNOWLEDGMENTS

We are indebted and deeply grateful to Randolph T. Williams, to an anonymous reviewer, and to the Associate Editor Bernhard Grasemann, whose precise criticisms and comments allowed us to greatly improve and sharpen this paper.

Mahtab Mozafari is warmly thanked for fruitful discussion concerning the interpretation of diagenetic and isotopic data. Federica Pessina is kindly acknowledged for the support during field work in the Crotone Basin. The authors wish also to thank Enrico Maria Selmo and Antonietta di Matteo for stable isotope analysis. Andrea Comelli and Luca Barchi are acknowledged for thin section preparation and support during scanning electron microscopy image acquisition, respectively. Cristian Cavozzi is thanked for technical support.

Author Contributions: Mattia Pizzati collected field and laboratory data, provided their interpretations, and wrote the manuscript; Fabrizio Balsamo participated in fieldwork, contributed to data interpretation, and critically revised the manuscript; Fabrizio Storti participated in some fieldwork, contributed to data interpretation, and critically revised the manuscript; Paola Iacumin contributed in the interpretation of isotopic data and critically revised the manuscript. Fondazione Cariparma is kindly acknowledged for having provided funding during the first author's three-years Ph.D course at University of Parma.

REFERENCES CITED

Ahlgren, S.G., 2001, The nucleation and evolution of Riedel shear zones as deformation bands in porous sandstone: Journal of Structural Geology, v. 23, p. 1203–1214, https://doi.org/10.1016/S0191-8141(00)00183-8.

Antonellini, M., and Aydin, A., 1994, Effect of faulting on fluid flow in porous sandstones: petrophysical properties: AAPG Bulletin, v. 78, p. 355–377, https://doi.org/10.1306/8D2B1B60-171E-11D7-8645000102C1865D.

Antonellini, M., Aydin, A., and Pollard, D.D., 1994, Microstructure of deformation bands in porous sandstones at Arches National park, Utah: Journal of Structural Geology, v. 16, p. 941–959, https://doi.org/10.1016/0191-8141(94)90077-9.

Antonioli, F., Ferranti, L., Lambeck, K., Kershaw, S., Verrubbi, V., and Dai Pra, G., 2006, Late Pleistocene to Holocene record of changing uplift rates in southern Calabria and northeastern Sicily (southern Italy, Central Mediterranean Sea): Tectonophysics, v. 422, p. 23–40, https://doi.org/10.1016/j.tecto.2006.05.003.

Aydin, A., 1978, Small faults formed as deformation bands in sandstone: Pure and Applied Geophysics, v. 116, p. 913–930, https://doi.org/10.1007/BF00876546.

Aydin, A., and Johnson, A.M., 1978, Development of faults as zones of deformation bands and as slip surfaces in sandstone: Pure and Applied Geophysics, v. 116, p. 931–942, https://doi.org/10.1007/BF00876547.

Aydin, A., and Johnson, A.M., 1983, Analysis of faulting in porous sandstones: Journal of Structural Geology, v. 5, p. 19–31, https://doi.org/10.1016/0191-8141(83)90004-4.

Ballas, G., Soliva, R., Sizun, J.P., Benedicto, A., Cavailhes, T., and Raynaud, S., 2012, The importance of the degree of cataclasis in shear bands for fluid flow in porous sandstone Provence, France: AAPG Bulletin, v. 96, p. 2167–2186, https://doi.org/10.1306/04051211097.

Ballas, G., Fossen, H., and Soliva, R., 2015, Factors controlling permeability of cataclastic deformation bands and faults in porous sandstone reservoirs: Journal of Structural Geology, v. 76, p. 1–21, https://doi.org/10.1016/j.jsg.2015.03.013.

Balsamo, F., and Storti, F., 2010, Grain size and permeability evolution of soft-sediment extensional sub-seismic and seismic fault zones in high-porosity sediments from the Crotone basin, southern Apennines, Italy: Marine and Petroleum Geology, v. 27, p. 822–837, https://doi.org/10.1016/j.marpetgeo.2009.10.016.

Balsamo, F., and Storti, F., 2011, Size-dependent comminution, tectonic mixing and sealing behavior of a "structurally oversimplified" fault zone in poorly lithified sands: Evidence for a coseismic rupture?: Geological Society of America Bulletin, v. 123, p. 601–619, https://doi.org/10.1130/B30099.1.

Balsamo, F., Storti, F., and Gröcke, D., 2012, Fault-related fluid flow history in shallow marine sediments from carbonate concretions, Crotone basin, south Italy: Journal of the Geological Society, v. 169, p. 613–626, https://doi.org/10.1144/0016-76492011-109.

Balsamo, F., Aldega, L., De Paola, N., Faoro, I., and Storti, F., 2014, The signature and mechanics of earthquake ruptures along shallow creeping faults in poorly lithified sediments: Geology, v. 42, p. 435–438, https://doi.org/10.1130/G35272.1.

Barnaby, R.J., and Rimstidt, J.D., 1989, Redox conditions of calcite cementation interpreted from Mn and Fe contents of authigenic calcites: Geological Society of America Bulletin, v. 101, p. 795–804, https://doi.org/10.1130/0016-7606(1989)101<0795:RCOCCI>2.3.CO;2.

Bense, V.F., Gleeson, T., Loveless, S.E., Bour, O., and Scibek, J., 2013, Fault zone hydrogeology: Earth-Science Reviews, v. 127, p. 171–192, https://doi.org/10.1016/j.earscirev.2013.09.008.

Bjørkum, P.A., and Walderhaug, O., 1990, Geometrical arrangement of calcite carbonate concretions within shallow marine sandstones: Earth-Science Reviews, v. 29, p. 145–161, https://doi.org/10.1016/0012-8252(90)90033-R.

Caine, J.S., and Minor, S.A., 2009, Structural and geochemical characteristics of faulted sediments and inferences on the role of water in deformation, Rio Grande Rift, New Mexico: Geological Society of America Bulletin, v. 121, p. 1325–1340, https://doi.org/10.1130/B26164.1.

Cashman, S., and Cashman, K., 2000, Cataclasis and deformation-band formation in unconsolidated marine terrace sand, Humboldt County, California: Geology, v. 28, p. 111–114, https://doi.org/10.1130/0091-7613(2000)28<111:CADFIU>2.0.CO;2.

Choi, J.-H., Edwards, P., Ko, K., and Kim, Y.-S., 2016, Definition and classification of fault damage zones: A review and a new methodological approach: Earth-Science Reviews, v. 152, p. 70–87, https://doi.org/10.1016/j.earscirev.2015.11.006.

Davatzes, N.C., Eichhubl, P., and Aydin, A., 2005, Structural evolution of fault zones in sandstone by multiple deformation mechanisms: Moab fault, southeast Utah: Geological Society of America Bulletin, v. 117, p. 135–148, https://doi.org/10.1130/B25473.1.

Davis, G.H., Bump, A.P., García, P.E., and Ahlgren, S.G., 2000, Conjugate Riedel deformation band shear zones: Journal of Structural Geology, v. 22, p. 169–190, https://doi.org/10.1016/S0191-8141(99)00140-6.

Davis, G.H., Reynolds, S.J., and Kluth, C.F., 2012, Structural Geology of Rocks and Regions: New York, USA, Wiley, 839 p.

Del Sole, L., and Antonellini, M., 2019, Microstructural, petrophysical, and mechanical properties of compactive shear bands associated to calcite cement concretions in arkose sandstone: Journal of Structural Geology, v. 126, p. 51–68, https://doi.org/10.1016/j.jsg.2019.05.007.

Demirdag, S., Yavuz, H., and Altindag, R., 2009, The effect of sample size on Schmidt rebound hardness value of rocks: International Journal of Rock Mechanics and Mining Sciences, v. 46, p. 725–730, https://doi.org/10.1016/j.ijrmms.2008.09.004.

Dickson, J.A.D., 1966, Carbonate identification and genesis as revealed by staining: Journal of Sedimentary Petrology, v. 36, p. 491–505.

Eichhubl, P., Davatzes, N.C., and Becker, S.P., 2009, Structural and diagenetic control of fluid migration and cementation along the Moab fault, Utah: AAPG Bulletin, v. 93, p. 653–681, https://doi.org/10.1306/02180908080.

Engelder, J.-T., 1974, Cataclasis and the generation of Fault Gouge: Geological Society of America Bulletin, v. 85, p. 1515–1522, https://doi.org/10.1130/0016-7606(1974)85<1515:CATGOF>2.0.CO;2.

Fagereng, Å., Hillary, G.W.B., and Diener, J.F.A., 2014, Brittle-viscous deformation, slow slip, and tremor: Geophysical Research Letters, v. 41, p. 4159–4167, https://doi.org/10.1002/2014GL060433.

Ferranti, L., Santoro, E., Mazzella, M.E., Monaco, C., and Morelli, D., 2009, Active transpression in the northern Calabria Apennines, southern Italy: Tectonophysics, v. 476, p. 226–251, https://doi.org/10.1016/j.tecto.2008.11.010.

Fossen, H., 2010, Structural Geology: New York, USA, Cambridge University Press, 463 p., https://doi.org/10.1017/CBO9780511777806.

Fossen, H., and Bale, A., 2007, Deformation bands and their influence on fluid flow: AAPG Bulletin, v. 91, p. 1685–1700, https://doi.org/10.1306/07300706146.

Fossen, H., Soliva, R., Ballas, G., Trzaskos, B., Cavalcante, C., and Schultz, R.A., 2018, A review of deformation bands in reservoir sandstones: Geometries, mechanisms and distribution, *in* Ashton, M., Dee, S.J., and Wennberg, O.P., eds., Subseismic-Scale Reservoir Deformation: Geological Society of London Special Publication 459, p. 9–33, https://doi.org/10.1144/SP459.4.

Friedman, I., and O'Neil, J.R., 1977, Compilation of stable isotope fractionation factors of geochemical interest: U.S. Geological Survey Professional Paper 440-KK, p. 1–117, https://doi.org/10.3133/pp440KK.

Friedman, M., and Logan, J.M., 1973, Lüders' bands in experimentally deformed sandstone and limestone: Geological Society of America Bulletin, v. 84, p. 1465–1476, https://doi.org/10.1130/0016-7606(1973)84<1465:LBIEDS>2.0.CO;2.

Galli, P., and Scionti, V., 2006, Two unknown M > 6 historical earthquakes revealed by palaeoseismological and archival researches in eastern Calabria (southern Italy). Seismotectonic implications: Terra Nova, v. 18, p. 44–49, https://doi.org/10.1111/j.1365-3121.2005.00658.x.

Giustini, F., Brilli, M., and Patera, A., 2016, Mapping oxygen stable isotopes of precipitation in Italy: Journal of Hydrology: Regional Studies, v. 8, p. 162–181, https://doi.org/10.1016/j.ejrh.2016.04.001.

Gratier, J.P., Richard, J., Renard, F., Mittempergher, S., Doan, M.L., Di Toro, G., Hadizadeh, J., and Boullier, A.M., 2011, Aseismic sliding of active faults by pressure solution creep: Evidence from the San Andreas fault observatory at Depth: Geology, v. 39, p. 1131–1134, https://doi.org/10.1130/G32073.1.

Hancock, P.L., 1985, Brittle microtectonics: Principles and practice: Journal of Structural Geology, v. 7, p. 437–457, https://doi.org/10.1016/0191-8141(85)90048-3.

Hendry, J.P., and Poulsom, A.J., 2006, Sandstone-hosted concretions record evidence for syn-lithification seismicity, cavitation processes, and Palaeocene rapid burial of Lower Cretaceous deep-marine sandstones (Outer Moray Firth, UK North Sea): Journal of the Geological Society, v. 163, p. 447–460, https://doi.org/10.1144/0016-764905-033.

Heynekamp, M.R., Goodwin, L.B., Mozley, P.S., and Haneberg, W.C., 1999, Controls on fault-zone architecture in poorly lithified sediment, Rio Grande Rift, New Mexico: Implications for fault-zone permeability and fluid flow, *in* Haneberg, W.C., Mozley, P.S., Moore, J.C., and Goodwin, L.B., eds., Faults and Subsurface Fluid Flow in the Shallow Crust: Washington D.C., USA, American Geophysical Union, Geophysical Monograph 113, p. 27–49, https://doi.org/10.1029/GM113p0027.

Hudson, J.D., 1977, Stable isotopes and limestone lithification: Journal of the Geological Society, v. 133, p. 637–660, https://doi.org/10.1144/gsjgs.133.6.0637.

Imanishi, K., Ando, R., and Kuwahara, Y., 2012, Unusual shallow normal-faulting earthquake sequence in compressional northeast Japan activated after the 2011 off the Pacific coast of Tohoku earthquake: Geophysical Research Letters, v. 39, p. 1–7, https://doi.org/10.1029/2012GL051491.

Kaproth, B.M., Cashman, S.M., and Marone, C., 2010, Deformation band formation and strength evolution in unlithified sand: The role of grain breakage: Journal of Geophysical Research. Solid Earth, v. 115, p. 1–11, https://doi.org/10.1029/2010JB007406.

Katz, O., Reches, Z., and Roegiers, J.C., 2000, Evaluation of mechanical rock properties using a Schmidt Hammer: International Journal of Rock Mechanics and Mining Sciences, v. 37, p. 723–728, https://doi.org/10.1016/S1365-1609(00)00004-6.

Katz, Y., Weinberger, R., and Aydin, A., 2004, Geometry and kinematic evolution of Riedel shear structures, Capitol Reef National Park, Utah: Journal of Structural Geology, v. 26, p. 491–501, https://doi.org/10.1016/j.jsg.2003.08.003.

Kim, Y.S., Peacock, D.C.P., and Sanderson, D.J., 2004, Fault damage zones: Journal of Structural Geology, v. 26, p. 503–517, https://doi.org/10.1016/j.jsg.2003.08.002.

Knott, S.D., and Turco, E., 1991, Late Cenozoic kinematics of the Calabrian Arc, southern Italy: Tectonics, v. 10, p. 1164–1172, https://doi.org/10.1029/91TC01535.

Kodaira, S., No, T., Nakamura, Y., Fujiwara, T., Kaiho, Y., Miura, S., Takahashi, N., Kaneda, Y., and Taira, A., 2012, Coseismic fault rupture at the trench axis during the 2011 Tohoku-oki earthquake: Nature Geoscience, v. 5, p. 646–650, https://doi.org/10.1038/ngeo1547.

Logan, J.M., Friedman, M., Higgs, N., Dengo, C., and Shimamoto, T., 1979, Experimental studies of simulated gouge and their application to studies of natural fault zones, *in* Speed, R.C., and Sharp, R.V., eds., Analysis of Actual Fault Zones in Bedrock: U.S. Geological Survey Open File Report 79-1239, p. 305–343.

Loveless, S., Bense, V., and Turner, J., 2011, Fault architecture and deformation processes within poorly lithified rift sediments, Central Greece: Journal of Structural Geology, v. 33, p. 1554–1568, https://doi.org/10.1016/j.jsg.2011.09.008.

Main, I., Kwon, O., Ngwenya, B., and Elphick, S., 2000, Fault sealing during deformation band growth in porous sandstone: Geology, v. 28, p. 1131–1134, https://doi.org/10.1130/0091-7613(2000)28<1131:FSDDGI>2.0.CO;2.

Mair, K., Main, I., and Elphick, S., 2000, Sequential growth of deformation bands in the laboratory: Journal of Structural Geology, v. 22, p. 25–42, https://doi.org/10.1016/S0191-8141(99)00124-8.

Mair, K., Elphick, S., and Main, I., 2002, Influence of confining pressure on the mechanical and structural evolution of laboratory deformation bands: Geophysical Research Letters, v. 29, p. 49-1–49-4, https://doi.org/10.1029/2001GL013964.

Mandl, G., 2000, Faulting in Brittle Rocks. An Introduction to the Mechanics of Tectonic Faults: Berlin, Germany, Springer, 434 p., https://doi.org/10.1007/978-3-662-04262-5.

Massari, F., and Prosser, G., 2013, Late Cenozoic tectonostratigraphic sequences of the Crotone Basin: Insights on the geodynamic history of the Calabrian arc and Tyrrhenian Sea: Basin Research, v. 25, p. 26–51, https://doi.org/10.1111/j.1365-2117.2012.00549.x.

Mitchell, T.M., and Faulkner, D.R., 2009, The nature and origin of off-fault damage surrounding strike-slip fault zones with a wide range of displacements: A field study from the Atacama fault system, northern Chile: Journal of Structural Geology, v. 31, p. 802–816, https://doi.org/10.1016/j.jsg.2009.05.002.

Mozley, P.S., and Goodwin, L.B., 1995, Patterns of cementation along a Cenozoic normal fault: A record of paleoflow orientations: Geology, v. 23, p. 539–542, https://doi.org/10.1130/0091-7613(1995)023<0539:POCAAC>2.3.CO;2.

Nelson, C.S., and Smith, A.M., 1996, Stable oxygen and carbon isotope compositional fields for skeletal and diagenetic components in New Zealand Cenozoic nontropical carbonate sediments and limestones: A synthesis and review: New Zealand Journal of Geology and Geophysics, v. 39, p. 93–107, https://doi.org/10.1080/00288306.1996.9514697.

Nicol, A., Childs, C., Walsh, J.J., and Schafer, K.W., 2013, A geometric model for the formation of deformation band clusters: Journal of Structural Geology, v. 55, p. 21–33, https://doi.org/10.1016/j.jsg.2013.07.004.

O'Leary, M.H., 1981, Carbon isotope fractionation in plants: Phytochemistry, v. 20, p. 553–567, https://doi.org/10.1016/0031-9422(81)85134-5.

Ogilvie, S.R., and Glover, P.W.J., 2001, The petrophysical properties of deformation bands in relation to their microstructure: Earth and Planetary Science Letters, v. 193, p. 129–142, https://doi.org/10.1016/S0012-821X(01)00492-7.

Olsson, W.A., Lorenz, J.C., and Cooper, S.P., 2004, A mechanical model for multiply-oriented conjugate deformation bands: Journal of Structural Geology, v. 26, p. 325–338, https://doi.org/10.1016/S0191-8141(03)00101-9.

Ozawa, S., Nishimura, T., Suito, H., Kobayashi, T., Tobita, M., and Imakiire, T., 2011, Coseismic and postseismic slip of the 2011 magnitude-9 Tohoku-Oki earthquake: Nature, v. 475, p. 373–376, https://doi.org/10.1038/nature10227.

Petit, J.P., 1987, Criteria for the sense of movement on fault surfaces in brittle rocks: Journal of Structural Geology, v. 9, p. 597–608, https://doi.org/10.1016/0191-8141(87)90145-3.

Philit, S., Soliva, R., Labaume, P., Gout, C., and Wibberley, C., 2015, Relations between shallow cataclastic faulting and cementation in porous sandstones: First insight from a groundwater environmental context: Journal of Structural Geology, v. 81, p. 89–105, https://doi.org/10.1016/j.jsg.2015.10.001.

Philit, S., Soliva, R., Castilla, R., Ballas, G., and Taillefer, A., 2018, Clusters of cataclastic deformation bands in porous sandstones: Journal of Structural Geology, v. 114, p. 235–250, https://doi.org/10.1016/j.jsg.2018.04.013.

Polonia, A., Torelli, L., Mussoni, P., Gasperini, L., Artoni, A., and Klaeschen, D., 2011, The Calabrian Arc subduction complex in the Ionian Sea: Regional architecture, active deformation, and seismic hazard: Tectonics, v. 30, p. 1–28, https://doi.org/10.1029/2010TC002821.

Rawling, G.C., and Goodwin, L.B., 2003, Cataclasis and particulate flow in faulted, poorly lithified sediments: Journal of Structural Geology, v. 25, p. 317–331, https://doi.org/10.1016/S0191-8141(02)00041-X.

Rawling, G.C., and Goodwin, L.B., 2006, Structural record of the mechanical evolution of mixed zones in faulted poorly lithified sediments, Rio Grande rift, New Mexico, USA: Journal of Structural Geology, v. 28, p. 1623–1639, https://doi.org/10.1016/j.jsg.2006.06.008.

Reitz, M.A., and Seeber, L., 2012, Arc-parallel strain in a short rollback-subduction system: The structural evolution of the Crotone basin (northeastern Calabria, southern Italy): Tectonics, v. 31, p. 1–23, https://doi.org/10.1029/2011TC003031.

Rotevatn, A., Torabi, A., Fossen, H., and Braathen, A., 2008, Slipped deformation bands: A new type of cataclastic deformation bands in Western Sinai, Suez rift, Egypt: Journal of Structural Geology, v. 30, p. 1317–1331, https://doi.org/10.1016/j.jsg.2008.06.010.

Scholz, C.H., 1998, Earthquakes and friction laws: Nature, v. 391, p. 37–42, https://doi.org/10.1038/34097.

Shipton, Z.K., and Cowie, P.A., 2001, Damage zone and slip-surface evolution over μm to km scales in high-porosity Navajo sandstone, Utah: Journal of Structural Geology, v. 23, p. 1825–1844, https://doi.org/10.1016/S0191-8141(01)00035-9.

Shipton, Z.K., and Cowie, P.A., 2003, A conceptual model for the origin of fault damage zone structures in high-porosity sandstone: Journal of Structural Geology, v. 25, p. 333–344, https://doi.org/10.1016/S0191-8141(02)00037-8.

Shipton, Z.K., Evans, J.P., and Thompson, L.B., 2005, The geometry and thickness of deformation-band fault core and its influence on sealing characteristics of deformation-band fault zones: in Sorkhabi, R., and Tsuji, Y., eds., Faults, fluid flow, and petroleum traps: AAPG Memoir, v. 85, p. 181–195.

Sigda, J.M., and Wilson, J.L., 2003, Are faults preferential flow paths through semiarid and arid vadose zones?: Water Resources Research, v. 39, p. 1–14, https://doi.org/10.1029/2002WR001406.

Sigda, J.M., Goodwin, L.B., Mozley, P.S., and Wilson, J.L., 1999, Permeability alteration in small-displacement faults in poorly lithified sediments: Rio Grande Rift, central New Mexico, *in* Haneberg, W.C., Mozley, P.S., Moore, J.C., and Goodwin, L.B., eds., Faults and Subsurface Fluid Flow in the Shallow Crust: Washington D.C., USA, American Geophysical Union, Geophysical Monograph 113, p. 51–68, https://doi.org/10.1029/GM113p0051.

Skurtveit, E., Torabi, A., Alikarami, R., and Braathen, A., 2015, Fault baffle to conduit developments: Reactivation and calcite cementation of deformation band fault in aeolian sandstone: Petroleum Geoscience, v. 21, p. 3–16, https://doi.org/10.1144/petgeo2014-031.

Soliva, R., Ballas, G., Fossen, H., and Philit, S., 2016, Tectonic regime controls clustering of deformation bands in porous sandstone: Geology, v. 44, p. 423–426, https://doi.org/10.1130/G37585.1.

Sternlof, K.R., Chapin, J.R., Pollard, D.D., and Durlofsky, L.J., 2004, Permeability effects of deformation band arrays in sandstone: AAPG Bulletin, v. 88, p. 1315–1329, https://doi.org/10.1306/032804.

Sylvester, A.G., 1988, Strike-slip faults: Geological Society of America Bulletin, v. 100, p. 1666–1703, https://doi.org/10.1130/0016-7606(1988)100<1666:SSF>2.3.CO;2.

Torabi, A., and Fossen, H., 2009, Spatial variation of microstructure and petrophysical properties along deformation bands in reservoir sandstones: AAPG Bulletin, v. 93, p. 919–938, https://doi.org/10.1306/03270908161.

Torabi, A., Braathen, A., Cuisiat, F., and Fossen, H., 2007, Shear zones in porous sand: Insights from ring-shear experiments and naturally deformed sandstones: Tectonophysics, v. 437, p. 37–50, https://doi.org/10.1016/j.tecto.2007.02.018.

Ujiie, K., and Kimura, G., 2014, Earthquake faulting in subduction zones: Insights from fault rocks in accretionary prisms: Progress in Earth and Planetary Science, v. 1, p. 1–30, https://doi.org/10.1186/2197-4284-1-7.

Van Dijk, J.P., 1994, Late Neogene kinematics of intra-arc oblique shear zones: The Petilia-Rizzuto Fault Zone (Calabrian Arc, Central Mediterranean): Tectonics, v. 13, p. 1201–1230, https://doi.org/10.1029/93TC03551.

Van Dijk, J.P., and Scheepers, P.J.J., 1995, Neotectonic rotations in the Calabrian Arc; implications for a Pliocene-Recent geodynamic scenario for the Central Mediterranean: Earth-Science Reviews, v. 39, p. 207–246, https://doi.org/10.1016/0012-8252(95)00009-7.

Van Dijk, J.P., Bello, M., Brancaleoni, G.P., Cantarella, G., Costa, V., Frixa, A., Golfetto, F., Merlini, S., Riva, M., Torricelli, S., Toscano, C., and Zerilli, A., 2000, A regional structural model for the northern sector of the Calabrian Arc (southern Italy): Tectonophysics, v. 324, p. 267–320, https://doi.org/10.1016/S0040-1951(00)00139-6.

Williams, R.T., Farver, J.R., Onasch, C.M., and Winslow, D.F., 2015, An experimental investigation of the role of microfracture surfaces in controlling quartz precipitation rate: Applications to fault zone diagenesis: Journal of Structural Geology, v. 74, p. 24–30, https://doi.org/10.1016/j.jsg.2015.02.011.

Williams, R.T., Goodwin, L.B., and Mozley, P.S., 2017, Diagenetic controls on the evolution of fault-zone architecture and permeability structure: Implications for episodicity of fault-zone fluid transport in extensional basins: Geological Society of America Bulletin, v. 129, p. 464–478, https://doi.org/10.1130/B31443.1.

Wilson, J.E., Goodwin, L.B., and Lewis, C.J., 2003, Deformation bands in nonwelded ignimbrites: Petrophysical controls on fault-zone deformation and evidence of preferential fluid flow: Geology, v. 31, p. 837–840, https://doi.org/10.1130/G19667R.1.

Yamaguchi, A., Sakaguchi, A., Sakamoto, T., Iijima, K., Kameda, J., Kimura, G., Ujiie, K., Chester, F.M., Fabbri, O., Goldsby, D., Tsutsumi, A., Li, C.F., and Curewitz, D., 2011, Progressive illitization in fault gouge caused by seismic slip propagation along a megasplay fault in the Nankai Trough: Geology, v. 39, p. 995–998, https://doi.org/10.1130/G32038.1.

Zecchin, M., Massari, F., Mellere, D., and Prosser, G., 2004, Anatomy and evolution of a Mediterranean-type fault bounded basin: The lower Pliocene of the northern Crotone Basin (Southern Italy): Basin Research, v. 16, p. 117–143, https://doi.org/10.1111/j.1365-2117.2004.00225.x.

Zecchin, M., Caffau, M., Civile, D., Critelli, S., Di Stefano, A., Maniscalco, R., Muto, F., Sturiale, G., and Roda, C., 2012, The Plio-Pleistocene evolution of the Crotone Basin (southern Italy): Interplay between sedimentation, tectonics and eustasy in the frame of Calabrian Arc migration: Earth-Science Reviews, v. 115, p. 273–303, https://doi.org/10.1016/j.earscirev.2012.10.005.

Science Editor: Wenjiao Xiao
Associate Editor: Bernhard Grasemann

Manuscript Received 20 March 2019
Revised Manuscript Received 30 June 2019
Manuscript Accepted 14 August 2019

Printed in the USA